

**GENERATING PATIENT-SPECIFIC 3D MODELS USING A
POINTING DEVICE**

by

THOMAS VAUGHAN

A thesis submitted to the
School of Computing
in conformity with the requirements for
the degree of Master of Science

Queen's University
Kingston, Ontario, Canada
August 2014

Copyright © Thomas Vaughan, 2014

Abstract

Computer assisted mosaic arthroplasty shows promise compared to traditional treatments of cartilage degeneration in the knee. It can be more accurate and less invasive, leading to improved outcomes. Computer assisted mosaic arthroplasty requires a computerized 3D model of the patient’s distal femur, normally generated from an Arthro-CT scan or MRI, but this process is associated with high cost, error, extended wait times, and radiation exposure. Our objective was to develop an alternative method to generate a 3D model intraoperatively within 1 mm error using points collected by a tracked pointing device. After generating the 3D model, we can optionally colour it according to a confidence metric. We validated our method in a user study where several orthopaedic surgeons and residents generated models of a rapid prototyped distal femur under different conditions. Our results suggest that it is possible to generate patient-specific 3D models with submillimeter accuracy using our method, and that this can be done within the time constraints of surgical procedures. We believe that the low error and minimal intraoperative time requirement may allow 3D model generation within the operating room without the need for any preoperative preparation.

Acknowledgments

Firstly, I would like to thank my supervisor Professor James Stewart for his continued mentorship and guidance throughout my Master's studies.

I would like to thank Kevin Birk and Matt Slonetsky for code which was shared among our projects. I would also like to thank many other colleagues in the laboratory for their support: Sai Bala, Matt Slonetsky, Kevin Birk, Ben Cecchetto, Jerome Grondin Lazazzera, Lucas Marcelli, Stephen Sebastyan, and Jiro Inoue.

I would like to thank Professor Gabor Fichtinger and Professor Randy Ellis for their mentorship and for helping me find my passion in computer assisted surgery.

Last, but certainly not least, my many friends and family for being there when I needed them. In particular, I thank my parents for everything they have done for me.

Contents

Abstract	i
Acknowledgments	ii
Contents	iii
List of Tables	vi
List of Figures	vii
Chapter 1: Introduction	1
1.1 Relevant Anatomy and Pathology	1
1.2 Treatments for Cartilage Degeneration	2
1.3 Shape of the Distal Femur	3
1.3.1 Segmentation Error	4
1.3.2 Registration Error	4
1.3.3 Other Considerations	4
1.4 Contribution	5
Chapter 2: Background	6
2.1 Data Acquisition	7
2.1.1 Pointing Devices	7
2.1.2 Endoscopes	9
2.1.3 Laser Scanning	10
2.1.4 Ultrasound	12
2.1.5 Radiographs	13
2.1.6 CT Scans	15
2.1.7 Simulated Data	16
2.2 Surface Generation	17
2.2.1 Function-based Methods	17
2.2.2 Atlas-based Methods	22

Chapter 3: Materials and Methods	27
3.1 Data Acquisition	27
3.1.1 Digitizing Probe	27
3.1.2 Tracking	28
3.1.3 Calibration	28
3.1.4 Surface Coordinate Frame	30
3.2 Surface Generation	30
3.2.1 Stage 1: Initial Outlier Filtering	31
3.2.2 Stage 2: First Surface Fit	31
3.2.3 Stage 3: Outlier Filtering Outside the Surface	33
3.2.4 Stage 4: Second Surface Fit	35
3.2.5 Stage 5: Surface Finalizing	35
3.3 Confidence Heatmap	37
Chapter 4: Experimental Validation	40
4.1 Parameter selection	40
4.2 Scanning surfaces	41
4.3 Experimental conditions	42
4.4 Subjects	42
4.5 Experimental setup	43
4.6 Experimental protocol	44
4.7 Alignment to Ground Truth	46
4.8 Evaluation Metrics	47
4.8.1 Visual Inspection	47
4.8.2 RMS Error	47
4.8.3 Data Acquisition Duration and Surface Mesh RMS Error	48
4.8.4 Data Acquisition Duration and Surface Generation Run Time	48
4.8.5 Questionnaire	48
Chapter 5: Results	49
5.1 Visual Inspection	49
5.2 RMS Error	53
5.3 Data Acquisition Duration and Surface Mesh RMS Error	53
5.4 Data Acquisition Duration and Surface Generation Run Time	53
5.5 Questionnaire	56
Chapter 6: Discussion	58
6.1 Specific Findings	58
6.1.1 Open Scans Compared to Arthroscopic Scans	58
6.1.2 Uncoloured Scans Compared to Heatmap Scans	59
6.1.3 Effect of Data Acquisition Duration	59

6.1.4	Ease of Using the Digitizing Probe	60
6.1.5	Surface Generation Failures	60
6.2	Limitations	61
6.2.1	Parameter Selection	61
6.2.2	Deviations from Validation Protocol	61
6.2.3	Sources of Error from Methods	62
6.2.4	Initial Surface Orientation	63
6.2.5	Code Errors	63
Chapter 7:	Conclusions	65
Bibliography		67
Appendix A: Informed Consent		77
Appendix B: User Study Questionnaire		81
Appendix C: Adjustments to Surface Generation		86
C.1	Initial Surface Orientation	86
C.2	Discontinuous Surfaces	87
C.2.1	Face Filtering: Normal Comparison	87
C.2.2	Face Filtering: Near Existing Points	87
C.3	Outlier Detection	88
C.4	Effect of Proposed Changes	88

List of Tables

4.1	Parameter selection for the user study	41
4.2	Task order	45
C.1	Modified parameter selection	88

List of Figures

2.1	Pointing device	7
2.2	Arthroscope	9
2.3	Radiograph segmentation	15
2.4	Hayashibe algorithm	19
3.1	Digitizing probe	28
3.2	NDI Polaris Spectra ®	29
3.3	Calibration	30
3.4	Surface generation flowchart	31
3.5	Surface generation: stage 1	32
3.6	Surface generation: stage 2	33
3.7	Surface generation: stage 3	34
3.8	Surface generation: stage 4	35
3.9	Surface generation: stage 2	38
3.10	Heatmap	39
4.1	Rapid prototyped models	42
4.2	Simulated skin	43
5.1	Surface meshes aligned to the ground truth	50

5.2	Failed surface generations	51
5.3	Surface meshes rendered with the confidence heatmap	52
5.4	Vertex error distribution	54
5.5	Data acquisition duration plotted against RMS error	55
5.6	Data acquisition duration plotted against surface generation run time	55
5.7	Questionnaire responses for usability	57
5.8	Questionnaire responses for confidence	57
C.1	Surface meshes using proposed changes	89
C.2	Failed surface generation	89

Chapter 1

Introduction

Cartilage repair in the knee is seeing increased importance with the growing aged population. Mosaic arthroplasty [23] is a cartilage repair technique, but it is highly technical and challenging [46]. Studies have shown that it can benefit from computer guidance [34, 53], but the shape of the distal femur needs to be known for computer guided methods to be used. A 3D model of the distal femur is typically obtained from a preoperative computed tomography (CT) scan, but this process is expected to introduce error, is costly, delays treatment, and exposes the patient to radiation. This thesis explores the problem of determining the shape of the distal femur intra-operatively without the use of a CT scan. The proposed method may be applicable for other anatomy.

1.1 Relevant Anatomy and Pathology

The knee joint consists of three bones: the femur, the tibia, and the patella. The femur connects the hip to the knee, and the tibia connects the knee to the ankle. The articular (contact) surfaces between these two bones form the knee joint. In a healthy knee, the articular surfaces are covered with lubricated hyaline cartilage and

slide smoothly.

The cartilage can become worn over time, or it can be damaged in a traumatic incident. Damaged cartilage, or damaged cartilage-plus-bone, can cause pain to the individual and can limit mobility. There is limited blood supply to the joint, so the cartilage surface will not regenerate. This condition is known as *cartilage degeneration*.

1.2 Treatments for Cartilage Degeneration

The typical treatment for cartilage degeneration is a knee replacement. A knee replacement involves replacing at least part of the knee joint with an implant. There are various methods by which this can be done, but ultimately a knee replacement is an irreversible, highly invasive procedure with a long recovery time. Furthermore, the implant has a limited lifetime of approximately 20 years [46], after which point a new implant must be put in, but with less likelihood of a successful outcome.

Cartilage repair techniques are intermediary procedures that can be performed before a knee replacement procedure is necessary. There are three cartilage repair techniques: stimulation of bone marrow, autologous cartilage implantation, and autologous chondrocyte implantation [46].

In marrow stimulation techniques, the bone is penetrated down to the marrow [43, 55]. The stem cells from the marrow rise to the articular surface, and form a layer consisting of fibrocartilage [60]. This type of cartilage has lower durability and different biomechanical properties than hyaline cartilage [38]. The recovery time (until normal activity can resume) is estimated to be from 4 to 6 months for the microfracture technique [55].

In autologous cartilage implantation [12, 39], two visits are required by the patient. In the first visit, the surgeon arthroscopically harvests a sample of hyaline cartilage. Additional cartilage is grown in a cell culture over several weeks. In the second visit, the cartilage is implanted to recreate the articular surface. The recovery time is 9 to 24 months. This is a costly procedure not only because of the requirement for two visits, but also because of the cell culture itself [46].

In mosaic arthroplasty [23], osteochondral plugs are collected from healthy, non-load bearing regions in the distal femur. The plugs are then transplanted to replace the worn or damaged cartilage. Normal daily activity can resume after 8 to 10 weeks, and regular activity can resume after 5 to 6 months. The disadvantage is this is a highly technical procedure that involves careful planning and precise execution.

Previous research has shown that computer assisted methods can improve the accuracy of mosaic arthroplasty [34, 53]. Furthermore, a plan for the procedure can be generated by a computer [29]. According to unpublished results in our lab, the plan can be generated in a time frame compatible with operating room constraints (one to two minutes). However, the shape of the distal femur must be known in order to generate this plan.

1.3 Shape of the Distal Femur

Presently, to determine the shape of the distal femur, the patient must undergo either an arthro-CT scan or a magnetic resonance imaging (MRI) scan. There are many reasons why either of these is undesirable, which will be discussed in the following subsections.

1.3.1 Segmentation Error

The shape is extracted from a scan by way of *segmentation*. The shape determined from a scan may contain inaccuracies due to *segmentation error*. These errors are difficult to quantify, since segmentation is often done manually and there will be variability from user to user. For automated methods, segmentation error has been estimated to be 0.18-0.24 mm in CT scans of sheep femurs [45]. Weese *et al.* [59] automatically segmented vertebrae to a mean error of 0.93 mm. We expect segmentation error to typically be a few tenths of a millimeter.

1.3.2 Registration Error

Intraoperatively, an iterative closest point algorithm [5] is used to find the transformation which aligns the 3D model to points on the anatomy surface. The alignment is not perfect, and contains some *registration error*. The error depends on the number of points collected on the surface of the anatomy, the distribution of the points, and on the amount of noise in the points. Registration error has generally been estimated to be in excess of a millimeter for orthopaedic surgery [28, 40, 57]. We therefore expect at least 1.0 mm from registration error.

1.3.3 Other Considerations

- An MRI scan or an arthro-CT scan has limited resolution, which affects the final segmented shape. Typically, the slice thickness is a few millimeters.
- An MRI scan or an arthro-CT scan introduces a treatment delay and extra cost.
- Arthro-CT scans involve injecting the patient with a contrast agent, which is

uncomfortable, requires a skilled radiologist, and has a potential for an allergic reaction.

- The patient is exposed to radiation from the arthro-CT scan.
- MRI is expensive and not always accessible.

1.4 Contribution

The contribution in this thesis is an alternative method for determining the shape of the distal femur. A tool is used to touch the distal femur surface during the operation in order to collect a 3D point cloud. The point cloud is then processed to build a 3D model. We also propose a method by which to colour the surface according to a confidence metric, so a surgeon knows where a denser point cloud might be needed. We perform a user study of surgeons and residents to determine the efficacy of this method in both open and arthroscopic surgery, and with or without the colour-coded confidence display.

The proposed method obviates the need for an arthro-CT or MRI scan. Furthermore, provided that the method is sufficiently accurate and fast, the entire procedure (scanning, planning, and execution) can be performed intraoperatively. The clinical requirement on error for the 3D model is presently unclear from the literature. Thus, our goal is to determine the shape of the distal femur within current acceptable bounds. Since the sum of segmentation and registration errors (Sections 1.3.1 and 1.3.2, respectively) is expected to be in excess of one millimeter, **our research objective was to generate a 3D model of the relevant parts of the distal femur with no more than 1mm error and without taking more than a few minutes of the surgeon's time.**

Chapter 2

Background

The goal is to intraoperatively produce a geometrical *mesh* describing the shape of a patient-specific anatomical surface, or simply a *surface mesh*. A mesh is a set of *vertices* (points), *edges* (lines), and *faces* (triangles) in three-dimensional space that together form a shape. The surface mesh is typically used for the planning and intraoperative guidance of surgery [14, 16, 17, 18].

Numerous methods have been proposed to generate surface meshes intraoperatively. We refer to this process as *scanning*. The surface being scanned is referred to as the *scanning surface*. Two distinct steps are performed as part of scanning: *data acquisition* and *surface generation*.

Data acquisition is the process of obtaining points that are near to or on the scanning surface. The resulting set of points is referred to as a *point cloud*. In some cases, other forms of data are collected, such as images [50]. The data is then used as the input to surface generation. Data acquisition will be described in more detail in section 2.1.

Surface generation is the process of constructing a surface mesh from the point

cloud. There are two types of surface generation: *function-based methods* and *atlas-based methods*. The former fits a mathematical function to the point cloud, whereas the latter makes use of *a priori* knowledge and deforms an existing mesh to the point cloud. Surface generation will be described in section 2.2.

2.1 Data Acquisition

Data acquisition in most cases involves finding a point cloud that is on or near to the scanning surface. Sometimes other types of data, such as images, can be collected [50]. Common methods for data acquisition are described in this section.

2.1.1 Pointing Devices

Many methods involve using a tracked *pointing device*, which physically contacts the scanning surface. The pointing device is calibrated such that the tip position is known with respect to a reference marker. An example of a pointing device is shown in Figure 2.1.



Figure 2.1: A tracked pointing device.

In Dessenne *et al.* [14], scanning is used to assist with anterior cruciate ligament

(ACL) replacement. A tracked pointing device is used to collect a point cloud on the surface of the proximal tibia. Julliard *et al.* [30] and Fleute *et al.* [16] also use pointing devices [14] for the same purpose. Rajamani *et al.* [44] use a pointing device on the proximal femur.

Sati *et al.* [51] describe a tracked Stille Hook, which is another pointing device similar to those described above. The Stille Hook features an angled tip, which allows the user to reach anatomy from various angles [51] and around obstructing tissue. Sati *et al.* are, to our knowledge, also the first researchers to consider tool bending. An embedded chip contains the factory-calibrated local coordinates of the tip with respect to a reference. Before each use, the tip is recalibrated. If the calibrated tip point ever moves more than 1 mm from the original calibrated tip point, the software will warn the user that the tool is bent and should not be used. Of particular interest in this work is the finding that use of the Stille Hook was easily learned.

In Stindel *et al.* [56], scanning is used to aid in knee replacement and intraoperative planning. Since using a sharp pointing device tip can cause damage to the scanning surface, a sphere-shaped tip with diameter 1 mm is used in this study. This allows the pointing device to slide over the scanning surface without scratching and damaging the articular surface. The exact point of contact with the scanning surface is not known since the calibrated point is the center of the sphere-shaped tip. The surface generation technique takes into account the radius distance offset of the point cloud from the scanning surface.

In this thesis, a tracked pointing device is used. No other specialized equipment is necessary. Our design features both an angled tip similar to Sati *et al.* [51], and a sphere-shaped tip similar to Stindel *et al.* [56].

2.1.2 Endoscopes

Endoscopes are specialized real-time cameras that are used transcutaneously (across the skin barrier). The camera is mounted inside a handle, and faces down into a long shaft with a lens. A scalpel is used to create a hole in the skin, and the shaft of the endoscope is inserted. This allows the surgeon to see anatomical structures beneath the skin and reduces the invasiveness, risk of infection, and recovery time of the procedure. In many orthopaedic procedures, a specialized endoscope called an *arthroscope* is used. The arthroscope shaft usually features a lens oriented off the shaft axis. This allows a greater range of possible views. An arthroscope is used in this thesis, and is shown in Figure 2.2. The tip is angled 30 degrees off the shaft axis.

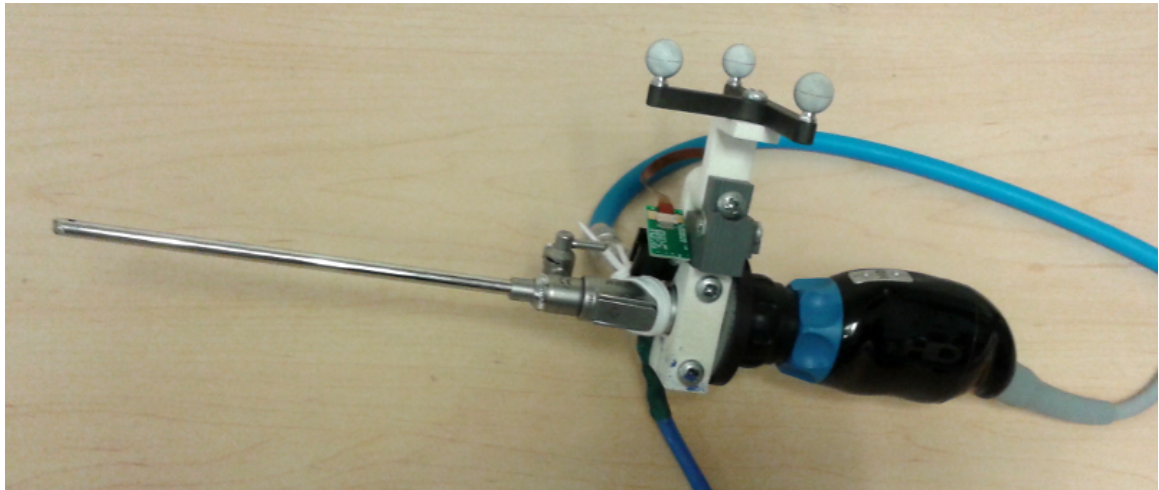


Figure 2.2: The arthroscope used in this thesis. Components are described in Section 4.5.

Endoscopes are used for data acquisition. There are two main methods to obtain point clouds from endoscopic video feeds: structure-from-shading and structure-from-motion.

Wu *et al.* [61] adopt a structure-from-shading approach for scanning a plastic spine

surface. Structure-from-shading involves inferring depth information from how light interacts with a scanning surface. Wu *et al.* [61] generate three-dimensional points from the two-dimensional endoscope image pixels. Depth information is initially expressed by light intensity as a function of the position in the camera image, but the data is smoothed and normals are also extracted.

In Hu *et al.* [27], a structure-from-motion approach is used. Structure-from-motion involves tracking visual landmarks within image feeds. Both camera movement and the positions of feature points are computed [22]. The method is validated experimentally on a phantom and on a heart *in vivo*.

Neither of these approaches is used in this thesis because there may be occluded regions where the endoscope will be unable to see, and because the shaft of an endoscope bends easily. Bending may cause difficulty in recovering point clouds relative to a separate external reference; thus a registration procedure would need to be applied.

2.1.3 Laser Scanning

Another popular method for intraoperative data acquisition involves the use of *laser scanning* technology. The most common technologies operate by projecting a pattern of light onto the scanning surface. The light may be visible or invisible to the naked eye. A camera at a known offset from the projector then detects the pattern. Based on where in the camera image the light pattern is detected, a depth position is computed. Typically, the scanning surface must be open, like in dentistry [36]. In Miga *et al.* [37], a laser scanner is mounted on a robotic arm and used to obtain a surface mesh of an exposed liver. In this thesis, such a mechanism would require that the knee be opened, so we do not use it.

However, some endoscopic laser scanning technologies exist which may be applicable to joint scanning [24, 52]. In Hayashibe *et al.* [24], a laser emitter is embedded within an endoscope to obtain a surface mesh of the liver. A monochrome camera and digital colour camera are also used in this system. All tools are inserted through trocars in a pigs abdomen. The cameras detect the laser pattern on the scanning surface in addition to some texture (colour) information. The intention is to render tools with respect to the resulting surface mesh.

In Schmalz *et al.* [52] a light projector and color camera are embedded within a cylindrical tube similar to an endoscope. The light projector emits onto the bone a structured light pattern which consists of multiple differently-coloured rings. The boundaries between rings are detected by the color camera, and depth information for individual points is extracted. The device is moved and tracked using a robotic arm system. One point cloud is collected for each image, so all the point clouds are registered using an iterative closest point algorithm [15]. The combined point cloud is used as input to surface generation. Experiments are carried out on a plastic cavity phantom, a colon phantom, and lamb trachea. The disadvantages with the described system are the requirement for robotic arm movements of fixed transformations (though the authors note that they will mitigate this later using motion tracking from a second camera), and occlusions from soft tissue.

Zheng *et al.* [66, 67] perform laser scanning to produce a surface mesh of the proximal femur, which is used as a gold standard in a validation experiment for another method.

2.1.4 Ultrasound

Ultrasound is used for data acquisition. Conventional B-mode ultrasound transducers are linear or curvilinear arrays of high frequency sound emitters and detectors. An image is computed based on the length of time it takes for an emitted sound to reflect off some surface and be received by the detectors. The received signal has an intensity that is proportional to the amplitude of the sound. The output is thus a two-dimensional image whose pixels are arranged relative to the array, and whose pixel intensities match the intensities of the received sound. The three-dimensional position of any given pixel can be determined when ultrasound transducers are spatially tracked by an external system.

It should be noted that there also exist A-mode ultrasound transducers and three-dimensional ultrasound transducers. A-mode ultrasound transducers consist of a single pencil beam ultrasound emitter and detector, and thus result in a one-dimensional image. Three-dimensional ultrasound transducers, as the name suggests, produce a three-dimensional image that gives more anatomical context, but these are often lower resolution than their A- or B-mode counterparts. Finally, ultrasound volumes can be constructed from series of tracked B-mode images [35].

In Chan *et al.* [9], points from the 3D ultrasound of a phantom femur are manually segmented. In a later work [8], Chan *et al.* manually segment tracked B-mode ultrasound images from three cadaver femurs and two cadaver hips. It is unclear how many points are typically obtained in either of these studies. Barratt *et al.* [3] continue the work of Chan *et al.* Points on tracked B-mode ultrasound images are segmented manually, and a cubic spline is used to interpolate a contour of a bone. Thus, additional points can be extracted from any given image. On average, over

1500 points over clinically accessible regions are used.

Rajamani *et al.* [44] collect point clouds on cast proximal femurs through use of an automatic ultrasound segmentation method [32].

Foroughi *et al.* [19, 20] perform automatic segmentation of ultrasound images on cadaver pelvises.

Boundaries of objects must usually be segmented in these images. Unfortunately, this is not feasible intraoperatively due to the length of time it takes to perform the segmentation. Automated and semi-automated algorithms exist for extracting features, but these have not yet been widely adopted, possibly due to insufficient evidence of reliability [3, 63].

In addition, ultrasound does not penetrate bone. When a bone is present in an ultrasound image, pixels beyond the bone surface become shadowed. In the case of mosaic arthroplasty, this may pose a challenge due to occluding bony parts of the joint. For instance, the patella is a bone that lies anterior to the distal femur, and it covers sites of interest where the surgeon may wish to scan.

2.1.5 Radiographs

Radiographs (commonly known as X-ray images) cannot directly produce point clouds. X-rays are emitted from the source and received along a two-dimensional detector. It should be noted that if a point on the radiograph is segmented, it does not correspond to a single position, but rather a ray.

Fluoroscopy is sometimes used, in which a radiograph is continually calculated and updated at interactive rates.

Fleute *et al.* [17, 18] have two requirements in order to infer a point cloud from

one or more radiographs. Firstly, the radiographs must be calibrated. The position of the source and detector must be known. Secondly, they need an atlas. An atlas is a mesh that generally matches the scanning surface and that can deform in a statistically-determined fashion according to known variations in surface geometry.

Points on the border of the scanning surface are segmented from the input radiograph. These are the *segmented rays*. Radiographs of the atlas are then simulated using the same calibration as the input. The goal is that the simulated radiographs resemble the input radiograph. The atlas is moved so that there is a reasonable alignment. Once the atlas is aligned, the so-called *apparent contours* of the atlas are extracted. These are the edges that, on the simulated radiograph, separate the atlas from its surroundings. Finally, three-dimensional points on the atlas can be found by locating the closest point on the apparent contours to each segmented ray. Points on the border of the scanning surface can be found by locating the closest point on each segmented ray to the set of apparent contours. Unfortunately, this approach may experience difficulty in constructing concave regions, since the apparent contour does not necessarily capture the full shape of those regions. This process is illustrated in Figure 2.3.

Zheng *et al.* [66] use calibrated radiographs to scan 23 femurs (one plastic and twenty two cadaver). Some of the test cases are considered pathological and others are not. Two orthogonal radiographs are used, one saggital and one coronal. This method is published again in a different paper [67], alongside other methods by the same authors.

Zheng *et al.* [64, 67] later use calibrated radiographs to scan eleven cadaveric femurs. Two experiments are performed: either two images (coronal and sagittal) are

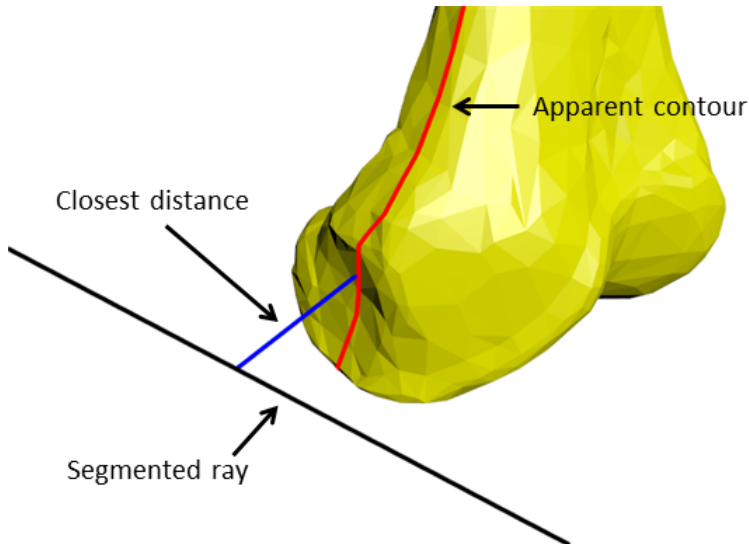


Figure 2.3: Fleute and Lavallée’s method [17]. The atlas is the yellow mesh. A segmented ray (black), the apparent contour (red), and the shortest distance between them (blue) are indicated.

used, or three images (coronal, sagittal, and intermediate) are used. The images are automatically segmented using an algorithm based on Canny edge detection [7].

It should be re-emphasized that this type of approach does require *a priori* knowledge and exposes the patient to radiation.

2.1.6 CT Scans

Although not generally used intraoperatively, *CT scans* can be computed from radiographs. To do this, a reverse-projection must be solved for every element in a three dimensional volume. It is common for CT scans to be preoperatively segmented to generate meshes of patient-specific anatomy. This process is typically not feasible intraoperatively due to the need for a CT scanner in the operating room, and the time required to perform manual segmentation.

Segmented meshes are often used as a gold standard for validation of scanning

techniques. There may be error in such meshes, however, due to segmentation error and the requirement to align a scanned surface with the gold standard [51, 56].

2.1.7 Simulated Data

Many studies use *simulated data*, where points are chosen on the surface of a known mesh. No physical scanning surface ever gets scanned; the process is entirely virtual. Errors caused by, for instance, tracking or segmentation can be simulated in a controlled fashion by the researchers. The exact scanning surface and its coordinate frame are known. There are no errors in the gold standard, such as user error during CT scan segmentation. This method, although not applicable to surgeries, gives a researcher the greatest control over validation. The results should be easily reproducible.

In the approach of Fleute and Lavallée [17], contour points are segmented from two orthogonal simulated radiographs on a known mesh of the distal femur. In a later work [18], several other data simulations are carried out for vertebrae. In the first experiment, intraoperative point cloud data (450 points) is simulated by dragging a virtual pointing device over the surgically accessible bone surface. In the second experiment, two x-rays are simulated on each of 10 known meshes similar to Fleute and Lavallée [17]. 400 points on the contour of the mesh are randomly segmented. In a final approach, a hybrid dataset consisting of points from both simulations is described. Soft tissue was not simulated.

In Zheng *et al.* [65, 67], point clouds of size 50 to 70 are simulated on the surfaces of each femur mesh. Some experiments include noise simulation, while others do not.

Mao *et al.* [36] use simulated laser scan data to reconstruct dental CAD models.

It is unclear how scanner inaccuracies are simulated during validation.

In Sadowsky *et al.* [50] three calibrated radiographs are simulated on eleven CT scans. In this approach, the images themselves are used as input to surface generation. Again, soft tissue is not simulated.

Grondin Lazazzera [21] uses simulated calibrated radiographs from CT scans. Several landmark features are segmented from these radiographs by human observers. The intersection between associated projected rays was used as a point.

The disadvantage with this type of approach is that it does not necessarily capture the variability that might occur if a scanning technique is used by different surgeons. Results of human use are also generally more convincing. Simulated data is therefore not used in this thesis. Rather, we construct phantoms with known geometry. The ground truth is available yet we still observe human interaction with the proposed system.

2.2 Surface Generation

There are two general types of surface generation techniques: *function-based methods*, and *statistical shape-based methods*. Function-based methods attempt to fit generalized functions to the input point cloud data, while statistical shape-based methods utilize *a priori* knowledge of the shape being generated.

2.2.1 Function-based Methods

A function-based method infers a mesh from the input point cloud and does not rely on *a priori* knowledge regarding the scanning surface. Function-based methods have seen wide use in fields such as range scanning, shape recognition, scene reconstruction from

series of images, and video game platforms. Many algorithms have been proposed, and reviews are provided by Berger *et al.* [4] and Chang [10]. Function-based methods have also been used to reconstruct anatomical shapes. This review will consider some of the most popular function-based methods applied to surface generation.

Two-dimensional Polynomials

In Dessenne *et al.* [14] and Julliard *et al.* [30], a point cloud is projected onto a least-squares fit plane. Point coordinates (x, y, z) are re-expressed in a different coordinate frame, where the x and y coordinates are positions of the projected points relative to the origin of the plane, and the z coordinate is the signed projection distance to the plane. A bicubic spline, $z = f(x, y)$ is fit to the re-expressed points to obtain a surface.

In Kunz *et al.* [33], four ordered points (and corresponding normals) on a mesh of a femoral condyle are chosen by an experienced operator, and the contained surface mesh is found through fitting a cubic spline. A cubic Hermite spline accurately represents the shape of the condylar surface. The error of the mesh compared to a gold standard (segmented CT scan) is 0.27 ± 0.09 mm.

Structured Points

In Hayashibe *et al.* [24], a point cloud on the liver surface is obtained from a laser scanner. The three-dimensional points are evenly distributed on a regular two-dimensional grid from the laser scanner's point of view (Figure 2.4a). Thus, the surface mesh is created by connecting two such triangles in each square within this grid (Figure 2.4b and Figure 2.4c). It is unclear whether it is possible for there to be points missing

from the grid. The algorithm only takes input from a single image, thus knowledge from previous images cannot be taken advantage of. During *in vitro* validation, a plane is imaged using the system. The average error from laser scanned points to the plane is 0.16 mm.

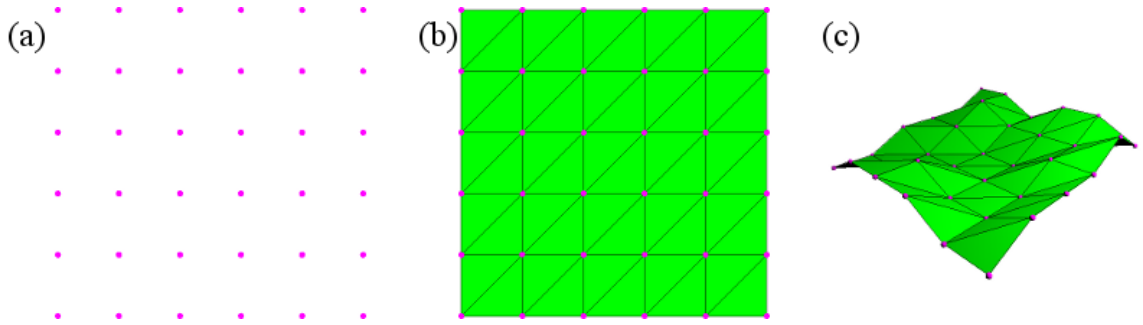


Figure 2.4: Algorithm by Hayashibe *et al.* [24] (a) Points (magenta) from the laser scanner’s point of view are shown. They form a regular grid. Each point has height information (not shown). (b) The points are triangulated (green). Each element within the regular grid becomes occupied by two triangles. (c) The resulting mesh is viewed from a different location.

In Wu *et al.* [61] the point cloud also appears as a regular two-dimensional grid from the endoscope’s point of view. Each point cloud was expressed as an image. Meshes from multiple images are aligned using the iterative closest point algorithm [5] and by incorporating an additional constraint that the normals and depths of points be globally consistent in all images.

Iterative Refinement

Mao *et al.* [36] use simulated laser scan data on teeth. The custom algorithm by Mao *et al.* for reconstructing the surface consists of (a) a two-dimensional Delaunay triangulation of projected points to find connectivity, (b) surface registration of multiple

meshes via an iterative closest point algorithm, (c) merging the meshes into an average shape via a volumetric algorithm, and (d) iterative surface refinement through a combination of smoothing the mesh and attracting mesh points back to raw data points. The average distance from the surface mesh to the ground truth is measured to be approximately 0.018 mm, which is comparable to at least one commercial platform. It is unclear whether such a low error could be achieved using real clinical data.

Structure-from-motion

In Hu *et al.* [27], a structure-from-motion approach is adopted using endoscopic data, meaning structure information is determined based on the movement of tracked features in the image feed. A three-dimensional geometrical model is obtained using a technique by Han and Kanade [22]. The method is applied to a heart phantom with known geometry from a CT scan. The reported experimental residual error after performing iterative closest point [5] to the gold standard is 1.68 mm.

Hoppe Reconstruction

In Hoppe *et al.* [26], a three-dimensional scalar function is estimated where the zero-set is considered to be the surface. The function is determined by a series of tangent planes inferred from the original point data. The planes consist of a centroid and a normal. To obtain the planes, for each point from the original data set, the nearest k neighbors are used to fit a plane in a least-squares sense. The normal of each plane may be oriented in one of two ways inward toward the surface or outward away from the surface. It is important for this normal orientation to be consistent across all

of the fitted planes. A graph is made where each node represents a point and plane pair, and the edges indicate the neighbors from the k neighborhood computation. The normal of a plane is propagated to all connected nodes on the graph according to a graph optimization algorithm. The three-dimensional function is generally calculated as the distance from any given sample coordinate to the nearest plane, but it can be considered undefined in cases where a user sets a threshold on plane distance. Finally, a marching cubes algorithm [62] is applied to extract the final surface from the function where it is equal to zero. This method is of particular interest because, apart from the coordinates of the points, no other information is needed (such as normals). The method described by Hoppe *et al.* was used in this thesis.

In Fleute *et al.* [16], a point cloud of size 6000 points undergoes Hoppe's algorithm [26] to generate a surface mesh of the distal femur. A postprocessing decimation algorithm [11] is applied to reduce the number of triangles.

In Sati *et al.* [51], a custom algorithm similar to Hoppe *et al.* [26] is used to generate surfaces from a point cloud on the distal femur, but the detailed description of the algorithm has not been published.

Poisson Reconstruction

Poisson reconstruction [31] is a more recent function-based method. The problem of surface reconstruction is defined as finding an indicator function (1 inside the shape, 0 outside the shape) whose gradient matches that of the known gradients at the sample points. This is cast as a Poisson problem in which the divergence of the gradient of the unknown indicator function must match the divergence of the gradient at the sample points. reformulated as a Poisson problem. The Laplacian term is equal to a vector

field determined using point normals. This approach requires normal information to be recorded along with the point positions.

In Schmalz *et al.* [52] point clouds undergo Poisson surface reconstruction [31] in order to obtain surface meshes. Only one experiment is carried out in Schmalz *et al.* where the geometry of the scanning surface (a generic cavity phantom) is known. The error is reported to be 0.092 mm.

2.2.2 Atlas-based Methods

Anatomical *atlases* see wide use in computer assisted systems [61, 25]. An atlas is a deformable mesh that can change shape to match a target input. For the purpose of illustration, the general implementation of Cootes *et al.* [13] is described. The atlas is constructed from several similar training shapes, which are each represented as points in high-dimensional space. Principal component analysis is used to reduce the dimensionality of the space and find statistically-correlated changes between meshes (known as modes of variation). The transform of the atlas and the weights for the modes of variation must be optimized in order to align the atlas to an input, which is usually a point cloud.

Other methods for atlas construction have been proposed, and the reader is referred to Heimann and Meinzer [25] for a thorough review.

Deformation based on Points

Fleute *et al.* [16] apply atlases to aid in anterior cruciate ligament replacement. A pointing device is used to digitize 11 dry cadaver femurs. The 11th model has a much denser point cloud and undergoes triangulation [26] so that it can act as a template

model. The other 10 point clouds are deformed and aligned to the template model based on an octree spline method developed by Szelski and Lavallée [58]. Principle components analysis is applied to the resulting displacements to obtain a statistical shape atlas. Fitting is performed on point clouds of size 100, and the residual fitting errors vary from 1.7 mm to greater than 2 mm depending on the number of modes of variation used during the fitting (0 to 6). In another experiment [18], Fleute *et al.* build an atlas from several segmented CT scans of vertebrae. They use a simulated pointing device on vertebrae and deform the atlas to fit the point clouds. They find the error is 1.2 mm.

Many other works take a similar approach. In Chan *et al.* [9], an anatomical atlas of the femur is generated from a segmented template CT scan which undergoes a non-rigid deformation alignment to 9 other CT scans as per Rueckert *et al.* [47]. The resulting displacement field is used to deform a mesh segmented from the template CT scan. The atlas is aligned to segmentated ultrasound points through two variations of the iterative closest point algorithm [2, 5, 42]. In a later work [8], Chan *et al.* extend the method to pelvises. The atlases are deformed according to manually segmented points from ultrasound scans to an error of 2 mm from the ground truth. Barratt *et al.* [3] continue the work of Chan *et al.* [8] and use a larger number of input points (usually over 1500), segmented from ultrasound. Errors to the ground truth are reported generally in excess of 2 mm. In Foroughi *et al.* [20], an atlas of the pelvis is also deformed to randomly distributed contour points on ultrasound images. The average global root mean square (RMS) error is reported to be 3.3 mm.

In Grondin Lazazzera [21], an anatomical atlas is constructed for the distal femur. During deformation, only the positions of a few landmark features in the distal femur

are used (as acquired from segmented simulated radiographs). The principal modes of variation are statistically estimated based on associated positions of landmark positions. The mean RMS error between corresponding points in a ground truth and surface mesh is reported to be 1.70 ± 0.37 mm.

In Zheng *et al.* [65, 67], an atlas is constructed from 30 proximal femurs. The fitting of the atlas is formulated as a three stage process: affine transformation, atlas deformation, and surface refining. The first two stages are similar to what has already been described. In the surface refining step, the surface is further subdivided according to a weight for thin-plate splines on the input point cloud [6]. This particular approach allows the atlas to capture pathology that is not necessarily reflected in the atlas training set. Point clouds of size 50 are simulated on the surfaces of input meshes, and the altas is deformed to those point clouds. Some experiments include noise simulation, while others do not. The errors are generally on the order of 0.5 mm to 0.6 mm, though the error is sometimes in excess of 2 mm. The two advantages of this method are the requirement for only a minimal point cloud of size roughly 50 and the ability to reconstruct pathology. The limitation in this study is that only simulated experiments are performed.

In Stindel *et al.* [56], a bone morphing algorithm is described. A statistical shape atlas of the femur is constructed using a method similar to Fleute *et al.* [16]. The point cloud is at an offset of roughly 0.5 mm from the surface because the pointing device features a sphere-shaped tip. The algorithm takes this offset into account. According to experiments, the accuracy of reconstructed points with relation to the ground truth surface is generally 0.5 mm RMS. A minimum of 500 points are required, and 1000 are recommended. Rajamani *et al.* [44] also apply an atlas to build a proximal femur

surface mesh with error 1.76 mm for pointing device data, and error in excess of 3mm for segmented [32] ultrasound data.

Deformation based on Radiographs

In Fleute *et al.* [17, 18], projection rays are segmented from the input radiographs. The points along the ray closest to the atlas, and the points on the atlas closest to the ray, are found as described in Section 2.1. The atlas is deformed so as to minimize the distance between these pairs of points. The error from the surface mesh to the ground truth for simulated data in the femur is reported to be 1.0 mm [17]. Error from surface mesh to ground truth for simulated data in the vertebrae is 0.62 mm [18]. Error from surface mesh to gold standard (registered, segmented CT scan) applied to vertebrae in a cadaver is 1.27 mm [18].

Zheng *et al.* [66, 67] use an atlas constructed similarly to a previous work [65]. Again, segmented radiographs are the input. Some of the 23 test cases are considered pathological and others are not. The reported mean error (from surface mesh to gold standard) is 0.95 mm. Some gold standards are determined through segmentation of a CT scan, and others are determined through use of a laser scanner reconstruction. Eleven more cadaveric femurs are scanned in Zheng *et al.* [64], and make use of either two or three automatically segmented radiographs. The error is reported to be 1.2 mm when two images are used, and 1.0 mm when three images are used.

In Sadowsky *et al.* [50] radiographs serve as the direct input to surface generation. The method attempts to best match the input radiograph to a simulation radiograph of the deformed atlas. This is achieved through a search procedure. The atlas in this study is constructed from a subset of 110 pelvis CT scans, where eleven are removed

randomly for the purposes of validation. The mean distance from the deformed atlas to a corresponding ground truth is 2 mm.

Hybrid Approaches

Finally, it should be noted that one experiment in Fleute *et al.* [18] uses both simulated radiographs and simulated pointing device data. The atlas is deformed according to the respective constraints for each type of data, and the resulting surface mesh to ground truth error is reported at 0.68 mm.

Limitations

Although they embed *a priori* knowledge regarding the scanning surface, atlases do have limitations. Zheng *et al.* [65, 66, 67] outline three limitations to the atlas-based methods in general:

- Extreme shapes that are not included in the training set will not be producible.
- Patient-specific pathology cannot be captured.
- There can be noise in the input point cloud.

Zheng *et al.* [64, 65, 66, 67] attempt to address some of these limitations using a surface refining technique.

Chapter 3

Materials and Methods

Our goal is to scan surfaces in the knee to obtain surface meshes. In order to do this, two problems need to be solved: data acquisition (Section 3.1) and surface generation (Section 3.2). A surface colouring enhancement is introduced in Section 3.3.

3.1 Data Acquisition

3.1.1 Digitizing Probe

We designed the *digitizing probe*, which is a tracked pointing device (Section 2.1.1). The tip is angled at 30 degrees to allow the surgeon to reach around obstructing tissue, similarly to Sati *et al.* [51]. The tip itself is sphere-shaped, which allows the tool to be slid over the scanning surface with minimized risk of damage due to scratching [56]. The radius of the sphere tip is 1.5 mm, and the length of the tip is 8 mm (including the sphere tip). The shaft of the digitizing probe is small enough to fit into an incision made for chisel or arthroscope insertion, which typically is 15-20 mm in size [54]. The handle has attached to it a reference marker, which can be detected by an external tracker. The digitizing probe is shown in Figure 3.1.



Figure 3.1: The digitizing probe used in this thesis. A close-up view of the tip is shown.

3.1.2 Tracking

The tracking system we use is the NDI Polaris Spectra ® (Figure 3.2, Northern Digital ®, Waterloo, Ontario, Canada), which we refer to as the *tracker*. The tracker consists of two infrared emitters and cameras. The tracker detects one or more reference markers within its field of view, and outputs *poses* for them, which are position and orientation pairs. Each reference marker therefore has an associated coordinate frame.

The tracker viewing volume is shaped like a truncated rectangular pyramid, with a near range of 950 mm, a far range of 2400 mm, a vertical angle of 16.58 degrees, and a horizontal angle of 13.66 degrees [41]. The tracker has an accuracy of 0.25 mm RMS according to the manufacturer [41]. The tracker collects 20 points per second.

3.1.3 Calibration

A calibration procedure was designed to determine the position of the digitizing probe's tip relative to the reference marker. The procedure involves constraining the sphere tip to a constant position within the tracker's field of view (Figure 3.3a), then rotating it around its tip while the tracker collects a series of reference marker



Figure 3.2: The NDI Polaris Spectra ⑧ (Northern Digital ⑧, Waterloo, Ontario, Canada) used in this study.

poses.

The distance from the sphere tip to the reference marker is constant (Figure 3.3b). Therefore, the tip is located at the center of a sphere fit to all of the reference marker positions. We use a least-squares sphere fitting algorithm to find this sphere and its center.

Due to noise, the center is not in a constant position relative to the reference marker coordinate frame. To address this, the center of the sphere is expressed in each of the reference marker coordinate frames. We use the mean of these center representations.

The calibrated point is at the center of the sphere tip. The points collected using the digitizing probe therefore lie at a offset of 1.5 mm from the scanning surface.

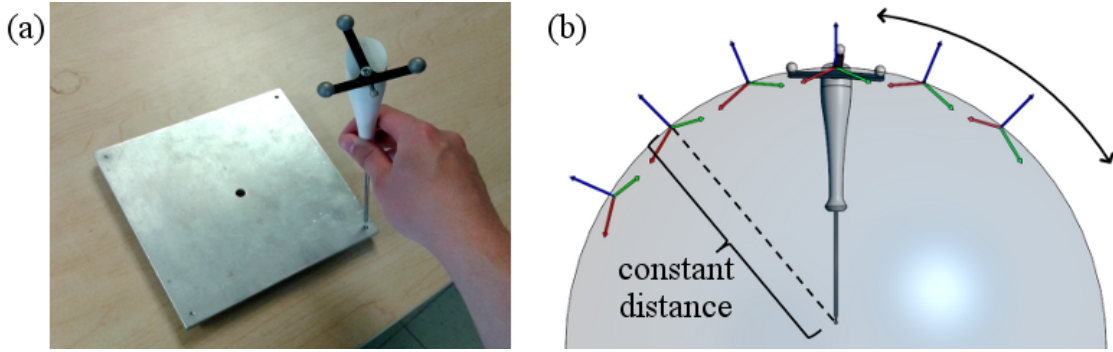


Figure 3.3: (a) A calibration plate is used to fix the digitizing probe’s tip to a constant position. (b) The distance from the reference marker to the fixed tip remains constant as the digitizing probe is rotated. The reference marker coordinate frames are indicated as the red, green, and blue lines.

3.1.4 Surface Coordinate Frame

A reference marker is attached rigidly to the scanning surface, and points are expressed in the coordinate frame of that reference marker. Thus, if the scanning surface moves, the points that have already been collected can still be correlated with new incoming points.

3.2 Surface Generation

Given a cloud of points collected in the surface coordinate frame, we wish to construct a surface mesh. The algorithm presented here consists of five stages. First, points which are in regions of low point density are detected and removed. Next, an initial surface is fit to the points. Then further outliers that are too far above the surface are removed. Another surface is fit to the remaining points and, in the final stage, the faces of that surface are offset, then further processed to extract the final surface mesh. This algorithm is shown in the flowchart below (Figure 3.4). Individual components of the algorithm are described in the subsections that follow.

The values for the parameters are given in the text below. We selected these values based on a pilot study, which is described in more detail in Section 4.1.

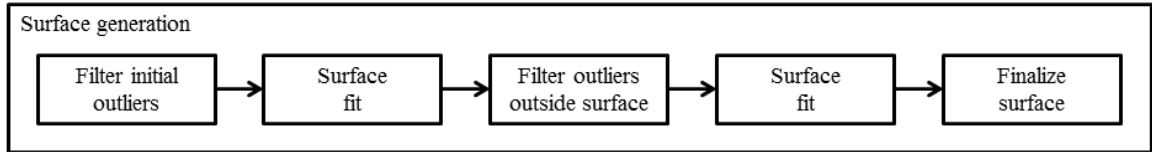


Figure 3.4: The stages involved in surface generation.

3.2.1 Stage 1: Initial Outlier Filtering

The input point cloud may contain outliers resulting from the tool slipping off the surface, or from brief periods of accidental acquisition (i.e. starting acquisition too soon, or stopping too late). Since these points may negatively affect the quality of the reconstruction, it is important to identify and remove them prior to further processing. The output from this stage of surface generation is a point cloud with detected outliers removed.

Outliers are detected and filtered based on the nearby point density (Figure 3.5). For each point in the input cloud, we count the number of points within a specified radius, $neighborCountRadius$ (we use a radius of 1 mm). If the number is greater than or equal to some threshold, $neighborCountThreshold$ (we use a threshold of 3 points), then the point is retained for further processing. Otherwise, the point is flagged as an outlier and is ignored in future processing.

3.2.2 Stage 2: First Surface Fit

In this stage, a surface is fit to the point cloud resulting from initial outlier filtering. The surface is a mesh, which we will refer to as the *initial surface*.

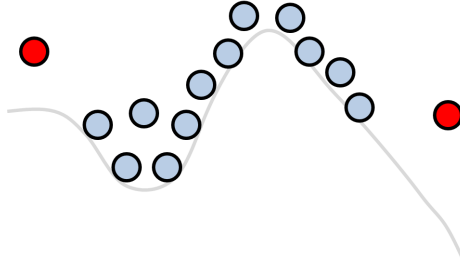


Figure 3.5: Initial outlier detection. The grey line is the scanning surface. Red circles represent detected outliers. Blue circles represent points that were kept.

Moving Least Squares Projection

The input point cloud will contain noise due to tracking error. The noise should be removed prior to an attempt at surface fitting. We used the *moving least squares* (MLS for short) projection implementation from PCL (the Point Cloud Library¹) [1, 48, 49]. For each input point, this technique will fit a local *mlsPolynomialOrder*-order polynomial function to nearby points within a specified radius, *mlsPolynomialRadius* (we use *mlsPolynomialOrder* = 3 and *mlsPolynomialRadius* = 10 mm). The point is projected to the polynomial surface (Figure 3.6a), thus removing noise.

Hoppe's Algorithm

Once the input point cloud has been projected, the surface reconstruction algorithm by Hoppe *et al.* [26] is used to produce the initial surface (Figure 3.6b). This algorithm is described in section 2.2.1. We refer to the parameter for the number of neighbors as *hoppeNumNeighbors* (we use 30 neighbors). We used the implementation from VTK (the Visualization Toolkit²) in the *vtkSurfaceReconstructionFilter* class. This

¹<http://pointclouds.org>

²<http://www.vtk.org>

initial surface does not yet take into account the radius of the sphere tip.

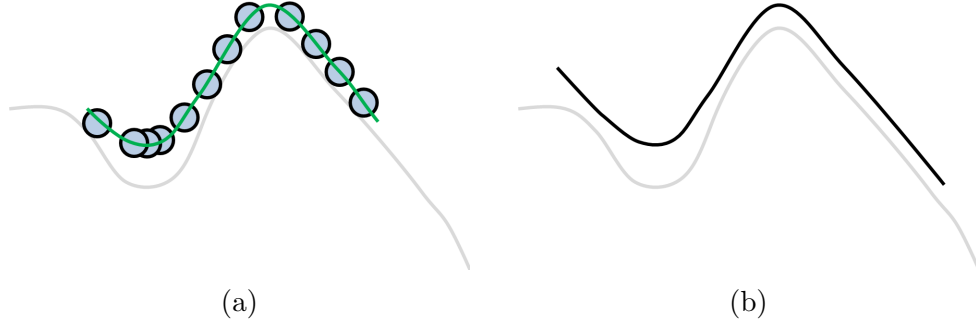


Figure 3.6: First surface fit. The grey line is the scanning surface. (a) Points (blue circles) are projected to locally fit MLS polynomials (green line) (b) Hoppe’s algorithm [26] is applied on the resulting points to produce a mesh (black)

Normal Consistency

Finally, the mesh normals may be oriented one of two ways - inward toward the scanning surface, or outward away from the scanning surface. In the former case, the mesh normals must be reversed such that they are pointing outward from the scanning surface. An experienced operator can, upon inspection, manually reverse all of the mesh normals, and the surface generation method must be run a second time.

3.2.3 Stage 3: Outlier Filtering Outside the Surface

We consider the input point cloud immediately after initial outlier filtering (stage 1). We flag a point as an outlier if it there is sufficient distance from the initial surface, and if it is outside the initial surface (outside points will be discussed below). The output of this stage is thus a point cloud with further outliers removed (Figure 3.7).

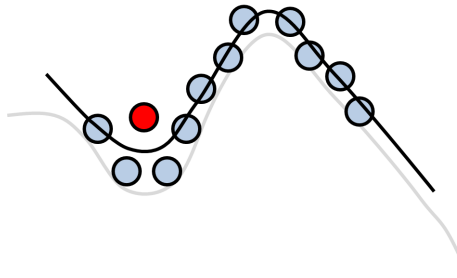


Figure 3.7: Further outlier filtering. The grey line is the scanning surface. Outliers (red circles) are detected outside the initial surface (black). Other points (blue circles) are kept for further processing.

Determining Distance

In order to determine the distance from any given point to the surface, we must find the *nearest surface point*. We define a nearest surface point as the position on the surface with the smallest distance to the given point. This nearest surface point can be a vertex in the surface, but this is not necessarily the case. The nearest surface point is found using the `vtkCellLocator` class from VTK. To find the distance, the length of the vector between the point and its nearest surface point is computed.

Determining Outside Points

Next, it must be determined whether the point is outside or inside the surface. The ray from the **input point** to the **nearest surface point** is computed. A dot product is computed between the ray direction and the surface normal. The dot product is negative if and only if the input point is outside the surface. Otherwise the point is inside.

Filtering Criteria

If a point is outside the surface, and the distance to the surface is greater than some threshold, *aboveSurfaceThreshold* (we use 0.75 mm) then the point is flagged as an outlier and is discarded. Points inside the surface are not filtered since this stage is intended only to remove outliers resulting from the tool slipping or accidental acquisitions. The tool cannot physically slip inside the scanning surface.

3.2.4 Stage 4: Second Surface Fit

With further outliers removed, a second surface can be fit to the point cloud (Figure 3.8). We refer to this mesh as the *refined surface*, which is the output of this stage. We use the same process and parameters described in Section 3.2.2 (stage 2).

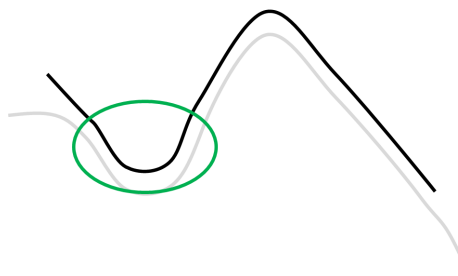


Figure 3.8: Second surface fit. The difference between the initial surface and the refined surface (black) is in the concave region (circled in green).

3.2.5 Stage 5: Surface Finalizing

At this stage, noise has been removed from the point cloud, and a refined surface has been fit to it. The true scanning surface, however, lies at an offset of 1.5 mm from the refined surface that has been computed thus far.

An offset surface from the refined surface is computed. The offset surface exists both outside and inside the refined surface (we use similar definitions for outside and inside as subsection 3.2.4). The surface mesh is a subset of the faces which lie inside the refined surface. There are two passes by which undesired faces are filtered out. Both passes make use of information acquired during MLS projection of stage 4.

Offset Surface

An *offset surface* from the refined surface is computed using the *vtkImplicitModeller* and *vtkContourFilter* classes from VTK (Figure 3.9a). Each point on the offset surface lies at a constant distance, *offsetDistance* from the refined surface (we use a 1.5 mm offset). There may be some error from tessellation due to the mesh representation, but the distance will remain generally constant.

The normals of the offset surface are initially oriented to face outward from the original refined surface. This is incorrect since, if this were to remain the case, the faces corresponding to the final surface mesh will have normals facing toward the inside of the scanning surface. The normals are reversed using the *vtkReverseSense* class from VTK.

Face Filtering: Normal Comparison

In the first pass of filtering, faces are removed based on the dot product with a single projection ray, the *expected normal*. The expected normal is directed out from the scanning surface.

To calculate the expected normal, we use information from the MLS projection in fitting the second surface. We remind the reader that during MLS projection, points

were projected to polynomial surfaces. For clarity, we will refer to these projection rays as *MLS rays*. The MLS rays from all inside points are added together, and then the result is normalized. This becomes the expected normal.

If the dot product of an offset surface face normal and the projection ray is positive, then the face is outside the refined surface and must be discarded. Otherwise, it is kept (Figure 3.9b).

Face Filtering: Near Existing Points

Unfortunately, the faces of the mesh extend beyond the scanned region. In addition, there still exist faces that “fold up” around the outer edges of the remaining offset surface. These outer regions should be removed.

In the second pass, an approximate convex hull around the MLS projected points is computed using VTK’s `vtkDelaunay3D` class (Figure 3.9c). Any offset face that is inside or within a threshold distance, `thresholdConvexHullDistance` (we use 2 mm), of the convex hull is retained for the final surface mesh. An offset surface face is considered within the threshold distance if any of its vertices are within the threshold distance of the convex hull.

After this pass of filtering, the remaining faces are the surface mesh (Figure 3.9d).

3.3 Confidence Heatmap

During scanning, surfaces that appear to be accurate may in fact contain errors resulting from insufficient point sampling. Unless indicated to the user, it may be difficult for the user to tell that this is the case. To address this problem the mesh is coloured according to nearby point density. Blue regions have dense sampling and

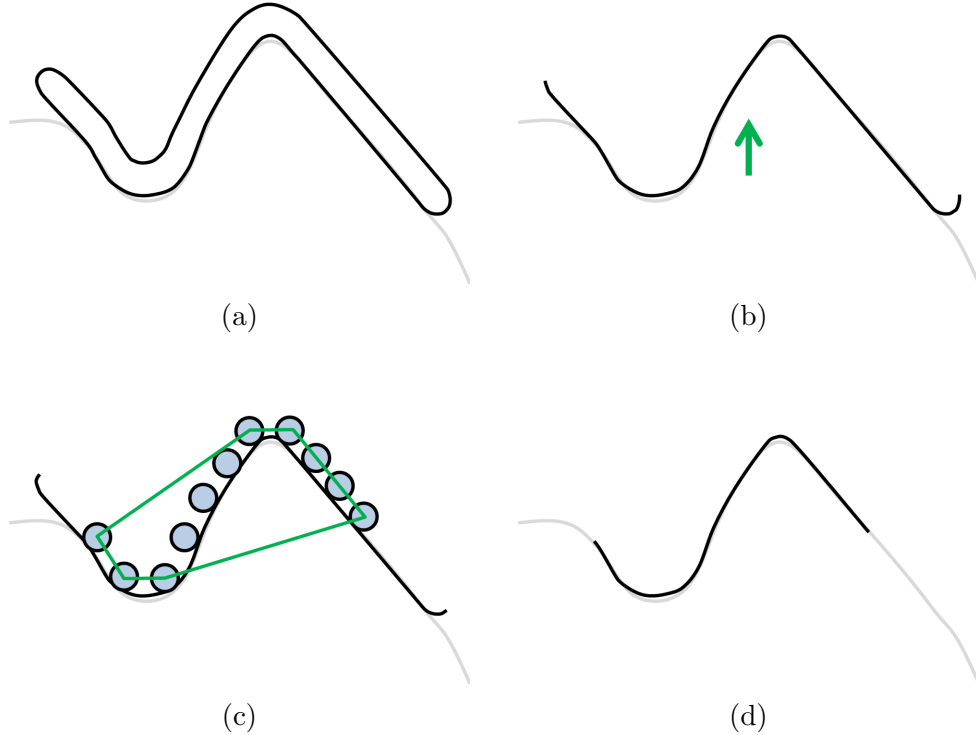


Figure 3.9: First surface fit. The grey line is the scanning surface. (a) The offset surface (black) is calculated (b) Faces are filtered based on the dot product with the expected normal (green arrow) (c) The convex hull of the projected points (blue circles) is shown (green) (d) The surface mesh (black) is the set of remaining faces

there is a high confidence that the surface mesh is accurate. Red regions have sparse sampling and there is a low confidence that the surface is accurate. We refer to this as the *confidence heatmap*.

At each vertex in the surface mesh, the number of nearby input points within a specified radius, *confidenceRadius* (we use 2 mm), is counted. If the number of points is less than or equal to a lower threshold, *confidenceLowerThreshold* (we use 0 points), the vertex is coloured red. If the number of points is greater than or equal to an upper threshold, *confidenceUpperThreshold* (we use 4 points), the vertex is

$\geq confidenceUpperThreshold$ (4 points)



$\leq confidenceLowerThreshold$ (0 points)

Figure 3.10: The range of possible colours for the confidence heatmap.

coloured blue. For any values in between, the colour is interpolated according to a heatmap (Figure 3.10).

Chapter 4

Experimental Validation

We wished to evaluate the proposed scanning method for use on the distal femur. In addition, we were interested to know whether the scanning method can be applied arthroscopically, and whether the confidence heatmap is useful during scanning. A user study was designed for these purposes.

4.1 Parameter selection

To determine the appropriate parameters for best surface reconstruction *prior* to the study, we did pre-study surface reconstructions. A surgeon performed data acquisition three times on one of our target sites on the knee (once open, twice arthroscopic). Data acquisition lasted between 30 and 70 seconds (600 to 1400 points). We manually optimized the parameters to minimize the distance from points to the refined surface, while also ensuring that acceptable surface meshes could be generated. The resulting parameter selections are shown in Table 4.1. These parameters were held constant for the subsequent user study.

For other anatomy, we would expect the parameters to be similar, but we would still need to optimize for the other anatomy separately.

Parameter Name	Value
<i>neighborCountRadius</i>	1 mm
<i>neighborCountThreshold</i>	3 points
<i>mlsPolynomialOrder</i>	3
<i>mlsPolynomialRadius</i>	10 mm
<i>hoppeNumNeighbors</i>	30
<i>aboveSurfaceThreshold</i>	0.75 mm
<i>offsetDistance</i>	1.5 mm
<i>thresholdConvexHullDistance</i>	2 mm
<i>confidenceRadius</i>	2 mm
<i>confidenceLowerThreshold</i>	0 points
<i>confidenceUpperThreshold</i>	4 points

Table 4.1: Parameter selection for the user study.

4.2 Scanning surfaces

Two models of the distal femur were rapid prototyped from the same mesh. The mesh was of a femur that needed to undergo mosaic arthroplasty in a real surgical case. On one model, the *reference model* (Figure 4.1a), three sites of clinical interest were marked:

1. A site near the lateral condylar ridge where cartilage can be taken from;
2. A site anterior to the intercondylar fossa where cartilage can be taken from,
and;
3. The site of the cartilage defect on the medial condyle.

The second model, the *scanning model* (Figure 4.1b), was fixed to a table and had attached to it a reference marker. This model was scanned during the user study.

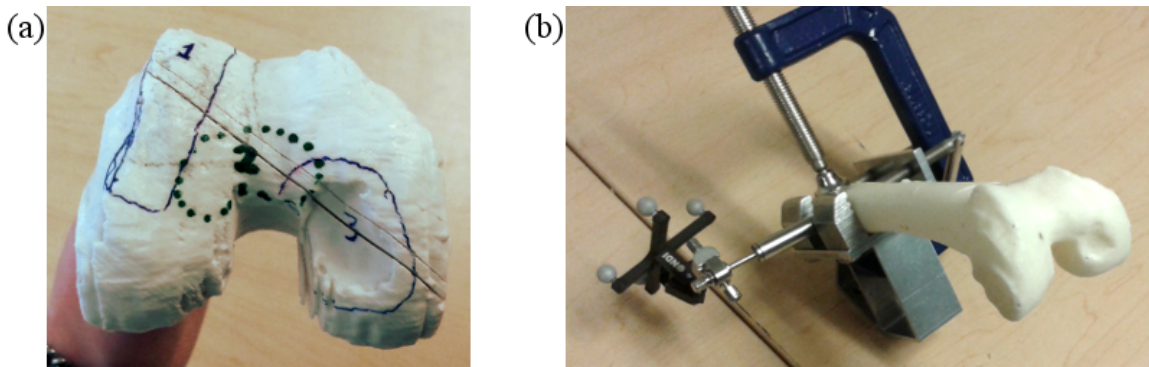


Figure 4.1: (a) The reference model with three sites of clinical interest marked. (b) The scanning model mounted on a table. A reference marker is attached to the scanning model.

4.3 Experimental conditions

The scanning model was scanned under all four combinations of two conditions: (1) scanning an **open** knee or scanning a covered knee **arthoscopically** (Figure 4.2); (2) displaying the confidence **heatmap** or displaying a plain **uncoloured** surface.

4.4 Subjects

Three orthopaedic surgeons (years of experience ranging from 2 to 15) and four orthopaedic residents (year of residency ranging from 1 to 4) were recruited from Kingston General Hospital. Each subject was assigned an identifier. Subjects 1, 6, and 7 were surgeons, and the remainder were residents. All subjects were right-handed.

Subject 1 had prior experience using the digitizing probe during a pilot study when we determined parameter selection (Section 4.1).

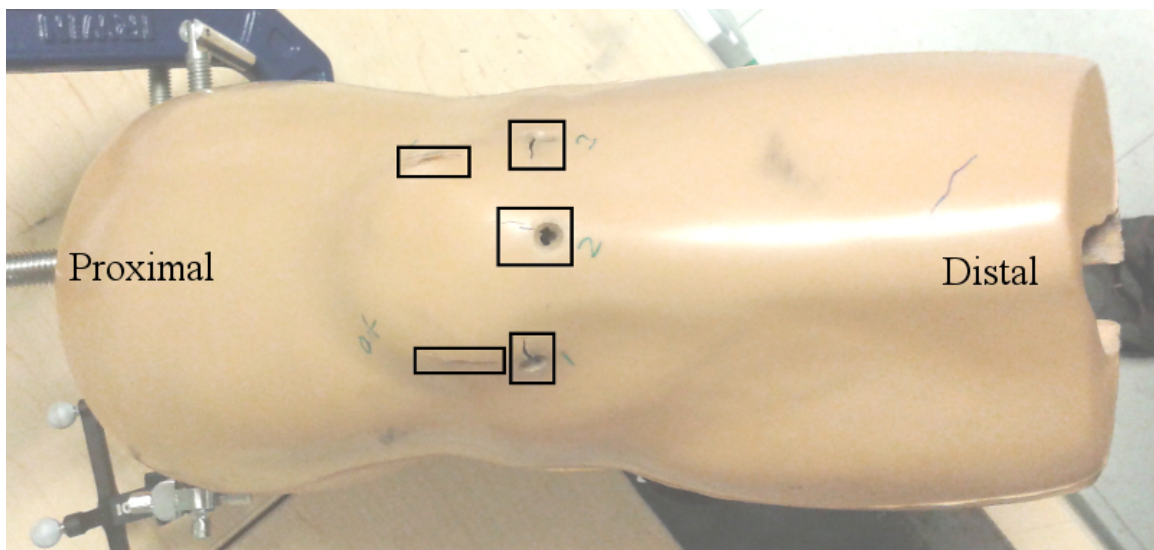


Figure 4.2: The simulated skin that was used to cover the scanning model, Sawbones® ACL Knee Trainer, ERP # 1413 (Sawbones®, Vashon Island, Washington, United States). Holes were made before the user study for insertion of instruments. These holes are indicated using black square boxes. The proximal and distal directions are marked.

4.5 Experimental setup

The experimental setup consisted of the tracker, the digitizing probe, an arthroscope (Figure 2.2) and visual display, a laptop, both scanning and reference models, and the simulated skin.

Subjects were given the reference model and told to use the digitizing probe to scan the corresponding specified sites on the scanning model. Each of the three sites was thus a scanning surface.

The arthroscope components were from Conmed Linvatec® (Conmed®, Largo, Florida, United States): a camera head (IM4121), a light guide (LG1050), a 4 mm 30 degree arthroscope (HD4301), a 5.5 mm sheath (QL5530), a camera controller (not shown, IM4000), and a light source (not shown, LS7700). Additional equipment has

been mounted on the arthroscope body as part of a concurrent experiment, including a reference marker which allows tracking.

The arthroscope head which can normally rotate about the shaft was locked in place as part of a concurrent experiment. The head normally allows the surgeon to have a wider range of possible views arthroscopically. It was infeasible to remove the lock between experiments due to time constraints. We asked subjects if this had an effect on their performance.

The laptop ran the software required for data acquisition (Section 3.1), surface generation (Section 3.2), and surface colouring (Section 3.3). Subjects performed data acquisition, and an operator ran surface generation on the laptop. The laptop had a quad-core 2.2 GHz CPU, and 8 GB of RAM. The software limited any continuous data acquisition to 30 seconds. The subject would examine the mesh after 30 seconds, and would decide if another 30 seconds were necessary to collect a denser point cloud. If not, then the next site would be scanned. Thus, most data collection times were in quanta of 30 seconds.

4.6 Experimental protocol

A *task* is defined as a scan on a single site under one of the experimental conditions. In order to avoid learning bias, a schedule was created so that no experimental condition or scanning site would consistently occur first, second, or so on. Each subject was assigned a different order in which to perform the tasks (Table 4.2).

The digitizing probe was calibrated before the subject performed his or her first scan. The digitizing probe was calibrated again after any series of arthroscopic tasks, since it was possible that the digitizing probe's shaft might bend.

Subject	1	2	3	4	5	6	7	8	9	10	11	12
1	AH1	AH2	AH3	AU1	AU2	AU3	OH1	OH2	OH3	OU1	OU2	OU3
2	OU2	OU3	OU1	OH2	OH3	OH1	AU2	AU3	AU1	AH2	AH3	AH1
3	AU3	AU1	AU2	AH3	AH1	AH2	OU3	OU1	OU2	OH3	OH1	OH2
4	OH1	OH2	OH3	OU1	OU2	OU3	AH1	AH2	AH3	AU1	AU2	AU3
5	OU2	OU3	OU1	AU2	AU3	AU1	OH2	OH3	OH1	AH2	AH3	AH1
6	AH3	AH1	AH2	OH3	OH1	OH2	AU3	AU1	AU2	OU3	OU1	OU2
7	OH1	OH2	OH3	AH1	AH2	AH3	OU1	OU2	OU3	AU1	AU2	AU3

Table 4.2: The order of tasks for each subject. Each task is denoted by three characters. The first character indicates an arthroscopic (A) or open (O) scan. The second character indicates an uncoloured (U) or heatmap (H) scan. The third character indicates the site number.

After we obtained informed consent (the consent form and letter of information are in Appendix A), subjects were instructed on how to use the digitizing probe to collect a point cloud. Subjects were allowed to acquire data for up to 30 seconds at a time. Subjects were encouraged to acquire data for the first full 30 seconds each time a new scan started.

During a practice period, subjects could scan any surface on the scanning model. Subjects were permitted to practice one open scan and one arthroscopic scan. The surface mesh was rendered on the laptop screen, which was oriented to face the subject. The surface was uncoloured during practice, since the intention was to demonstrate the workflow and to acquaint the subject with the digitizing probe.

Once the practice session was complete, the subject was asked to perform each task according to their schedule. Upon completion of all the tasks, the subject was asked to complete a questionnaire (Appendix B).

4.7 Alignment to Ground Truth

After the user study, we aligned each generated surface mesh to the ground truth in a two-step procedure.

We removed the outermost ring of vertices by removing any face which was connected to an outer vertex, since these vertices were unreliable and would not be used in clinical practice. An outer vertex was one that was connected to an edge that was connected to only one face. We repeated this two more times, so in total three rings of vertices are removed. This corresponded to approximately 3 mm of surface removed from the outside of each mesh, but the exact amount was variable depending on tesselation.

The iterative closest point algorithm [5] from VTK was used to align surface meshes to the ground truth. For each subject and experimental condition, the three surface meshes were placed in a common coordinate system in order to get a more accurate alignment. The iterative closest point algorithm ran for 100 iterations.

4.8 Evaluation Metrics

Whenever applicable, a one-tailed Wilcoxon signed rank test for paired data was used to determine statistically significant difference. We used the Pearson correlation coefficient squared (r^2) to report correlation between variables. We consider $p < 0.05$ to be statistically significant.

4.8.1 Visual Inspection

We visually inspected the aligned surface meshes to ensure that the iterative closest point algorithm was successful, and also to see if the surface generation method constructed surface meshes with appropriate shapes. To provide better context, these visualizations included the outer faces which were removed earlier.

4.8.2 RMS Error

Vertices from surface meshes were projected on to the nearest surface point on the ground truth using the *vtkCellLocatorClass* in VTK. The projection distance was considered the *signed vertex error*. We compute the RMS of these errors (RMS error).

For each condition, we reported the mean RMS error \pm standard deviation. We also plotted histograms showing the vertex error distribution for each combination of

conditions.

4.8.3 Data Acquisition Duration and Surface Mesh RMS Error

We plotted the duration of data acquisition against the RMS errors of the surface meshes.

4.8.4 Data Acquisition Duration and Surface Generation Run Time

We plotted the duration of data acquisition against the running time of surface generation. In cases where the operator decided that the initial surface normals needed to be reversed (Section 3.2.3) and the surface generation needed to run again, we reported the latter running time.

4.8.5 Questionnaire

Finally, subjects were given a questionnaire in order to acquire feedback regarding the usability of the system, their confidence of having scanned the relevant surfaces, and whether or not the confidence heatmap was useful.

Chapter 5

Results

5.1 Visual Inspection

We subjectively determined that the iterative closest point [5] alignments appeared correct. Examples of three of the aligned surfaces are shown in Figure 5.1.

In a limited number of cases (13 out of 81 surfaces total), the surface generation method produced incorrect shapes. We subjectively made this determination when the surface mesh contained holes or continuous faces which were not part of the ground truth. These discontinuities always occurred on either site 2 or site 3. Examples are shown in Figure 5.2.

Figure 5.3 shows examples of the confidence heatmap that was shown to the subjects.

Data acquisition from Subject 7 for one of the experimental conditions (open, uncoloured) was not completed because the operator did not save the data.

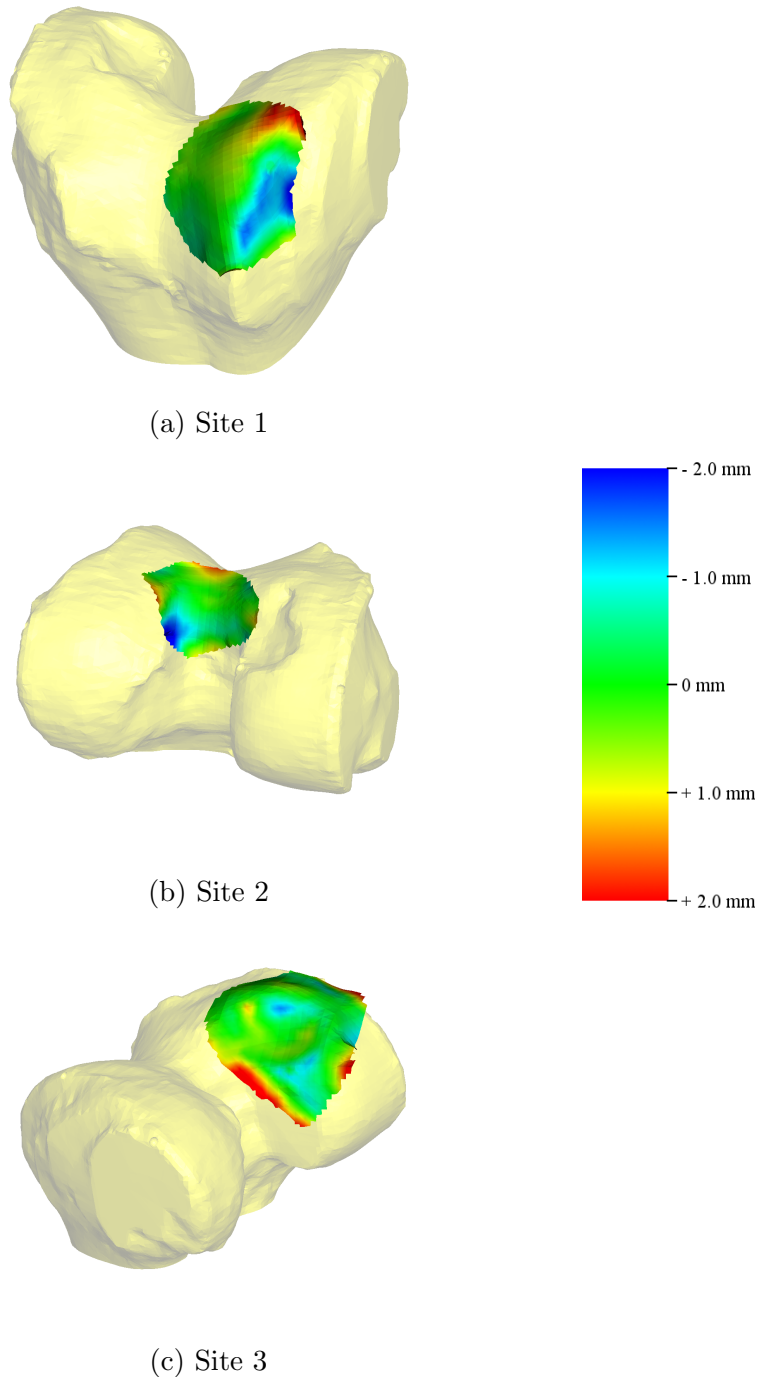


Figure 5.1: Examples of surface meshes produced by our system. The ground truth is shown behind the meshes for comparison. The colours indicate the signed distance from the ground truth (the scale is on the right).

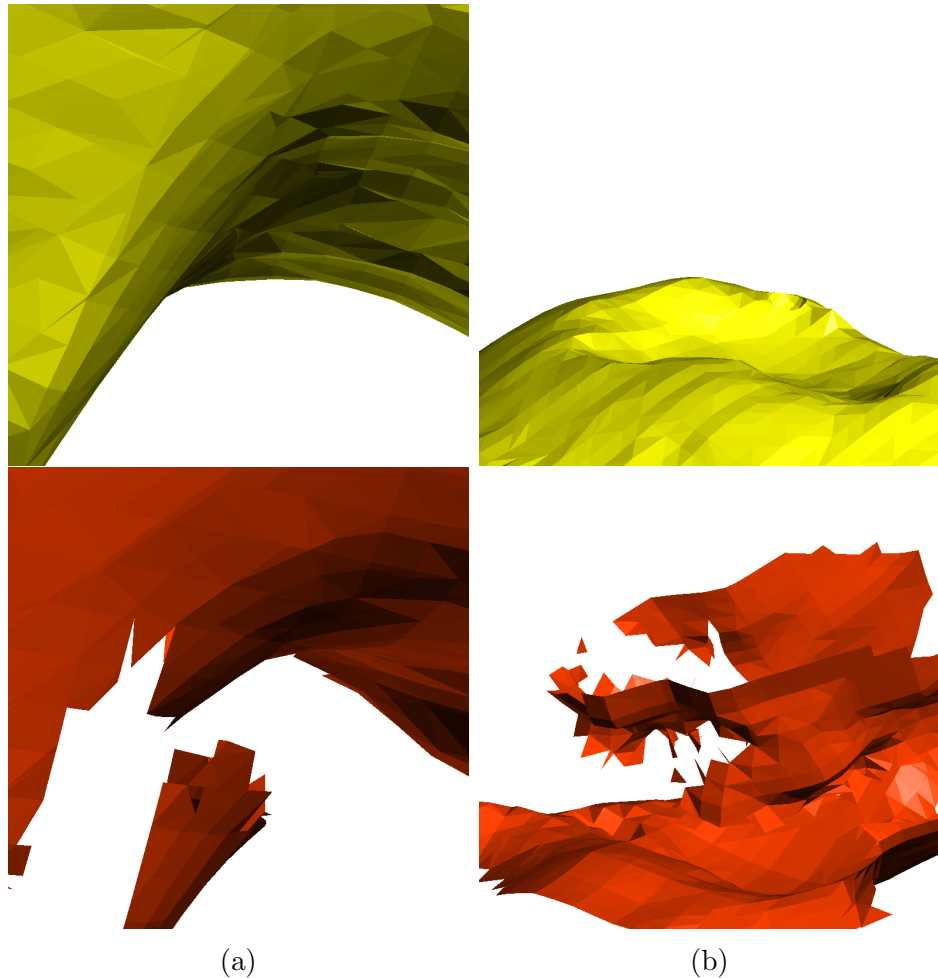


Figure 5.2: Examples of incorrect shapes produced by the surface generation method. Top: Ground truth mesh viewed from different angles. Bottom: Surface meshes viewed from matching angles. (a) A discontinuous surface in site 2. (b) The mesh *snakes* back on itself in site 3.

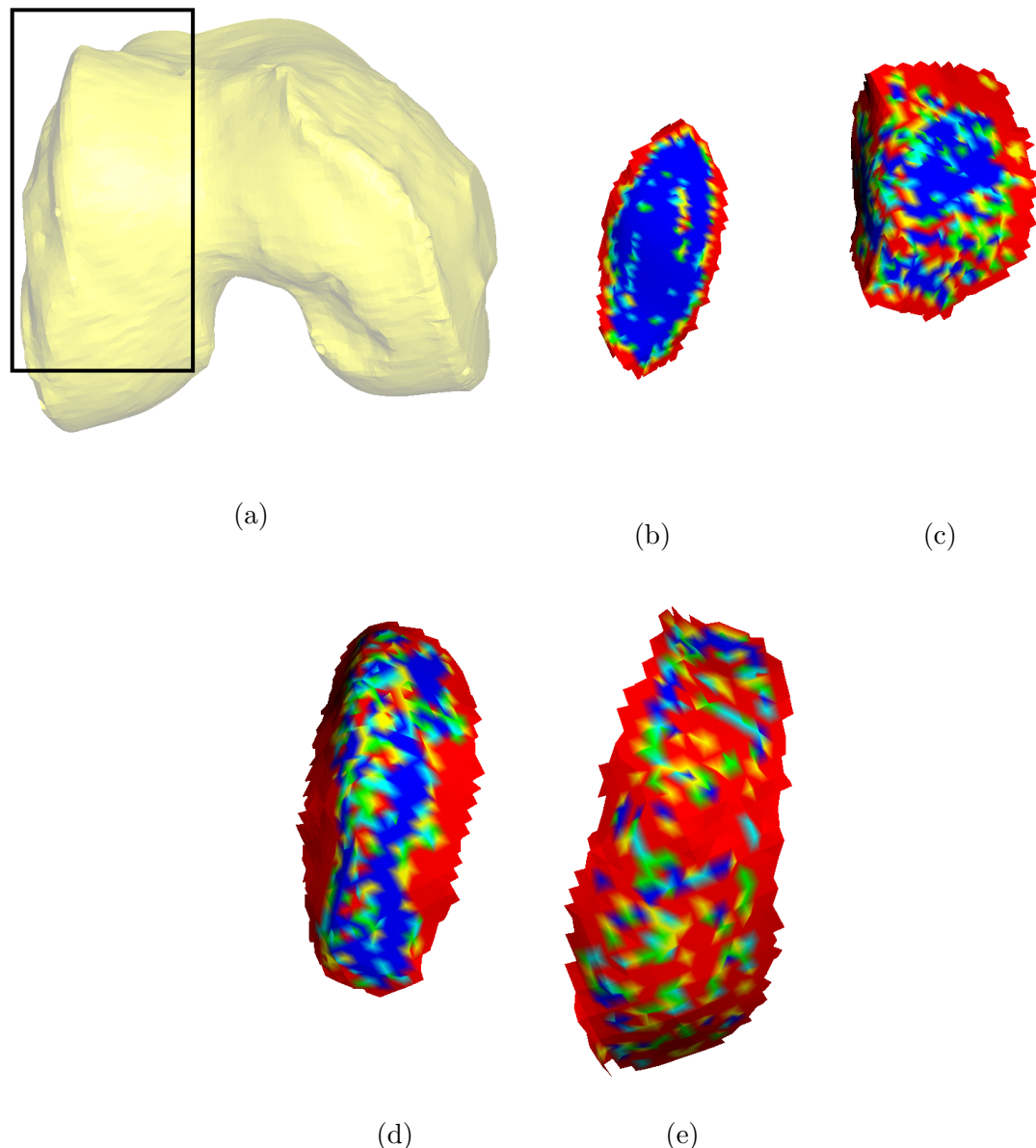


Figure 5.3: Surface meshes rendered with the confidence heatmap (Figure 3.10), as seen by the subject. (a) Ground truth reference. (b-e) Examples.

5.2 RMS Error

The main result is that this method can produce surface meshes with less than 1.0 mm RMS error within two minutes of scanning.

Surface meshes from open scans had a significantly lower mean RMS error (0.61 ± 0.36 mm, maximum 2.0 mm) than those produced arthroscopically (0.97 ± 0.58 mm, maximum 3.1 mm), with $p = 0.00015$.

Surface meshes from uncoloured scans did not have a statistically significantly higher mean RMS error (0.78 ± 0.52 mm, maximum 3.1 mm) than those produced using the heatmap (0.77 ± 0.52 mm, maximum 2.0 mm), with $p = 0.27$.

Histograms showing the distributions of signed vertex errors are shown in Figure 5.4.

5.3 Data Acquisition Duration and Surface Mesh RMS Error

Data acquisition duration (seconds) was plotted against the RMS error (mm) for each mesh (Figure 5.5). No statistically significant correlation was found ($r^2 = 0.0036, p = 0.60$).

5.4 Data Acquisition Duration and Surface Generation Run Time

Surface generation ran for 2.0 seconds on average. Surface generation was plotted against data acquisition duration (Figure 5.6). A significant positive correlation was found ($r^2 = 0.73, p < 0.0001$).

The shortest surface generation running time was 0.88 seconds, and the longest was 9.2 seconds. The mean was 2.0 seconds.

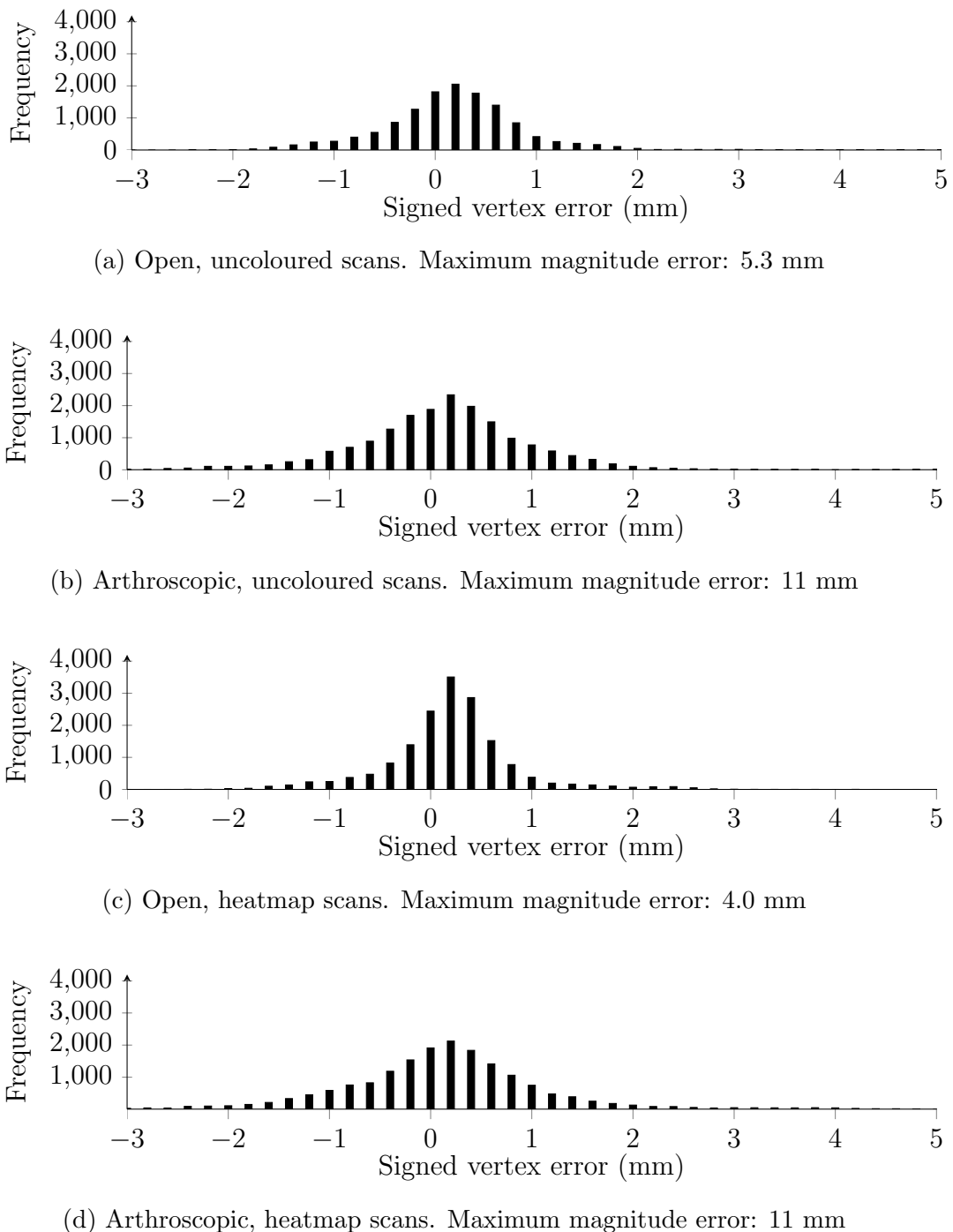


Figure 5.4: Vertex error distributions for each experimental condition pair. The maximum magnitude error for each condition pair is indicated under each histogram.

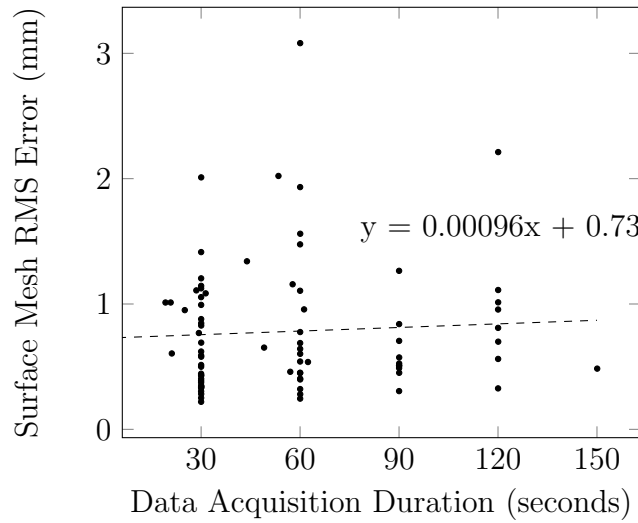


Figure 5.5: Data acquisition duration plotted against RMS error. The dashed line shows a linear best fit. No statistically significant correlation was observed ($r^2 = 0.0036, p = 0.60$).

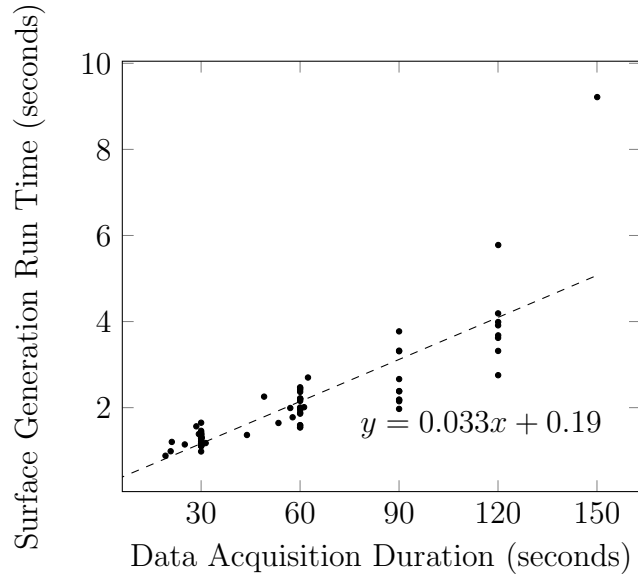


Figure 5.6: Data acquisition duration plotted against surface generation run time. The dashed line shows a linear best fit. Significant correlation was observed ($r^2 = 0.73, p < 0.0001$).

5.5 Questionnaire

Questions regarding the usability of the system were posed as agree/disagree statements with a five-point Likert scale. Subjects' responses are reported in Figures 5.7 (questions regarding usability) and 5.8 (questions regarding confidence).

The statistically significant findings were:

- Subjects reported that it was easier to keep the digitizing probe's reference marker within the tracker's view in open scans than in arthroscopic scans ($p = 0.016$).
- Subjects reported that it was easier to scan with the digitizing probe in open scans than in arthroscopic scans ($p = 0.031$).
- Subjects reported higher confidence in scanning all necessary surfaces in open uncoloured surfaces than in arthroscopic uncoloured surfaces ($p = 0.031$).

Subjects were also asked whether the fact that the arthroscope head was locked had an effect on their performance. Five subjects reported that it did.

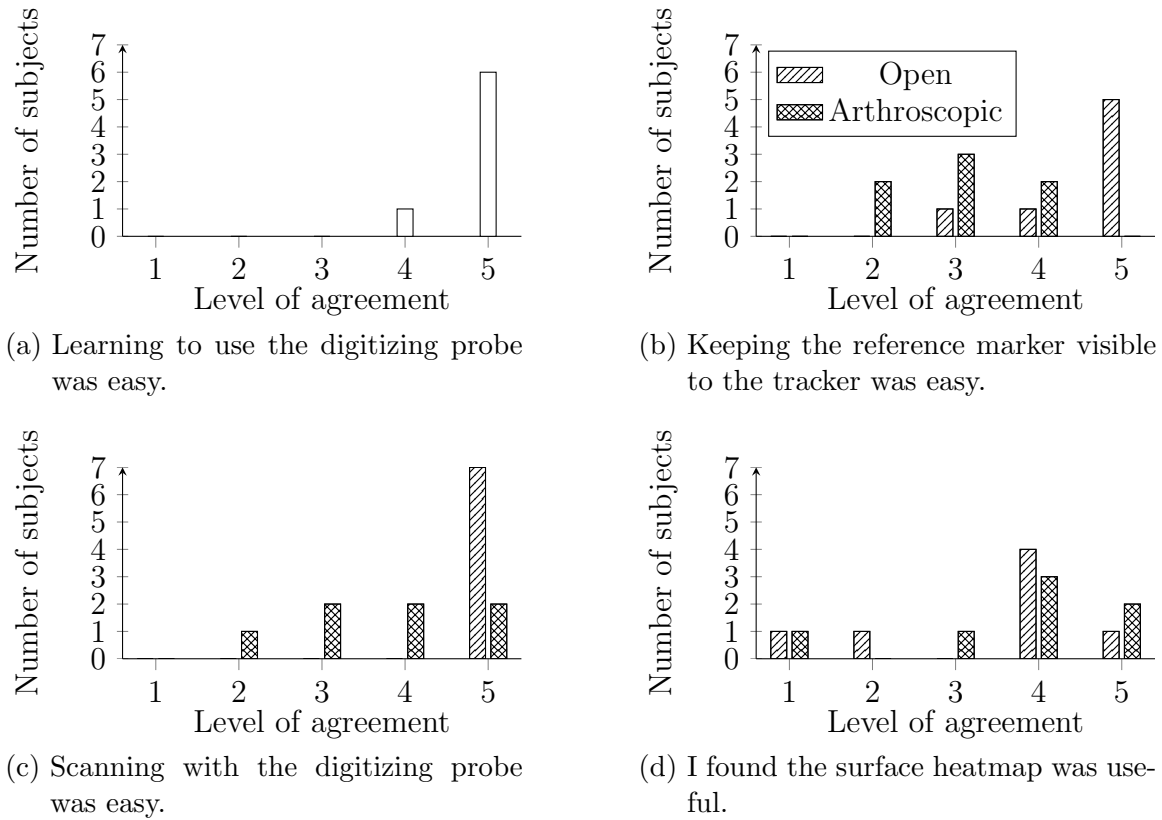


Figure 5.7: Level of agreement (1 = strongly disagree, 5 = strongly agree) to questions regarding usability.

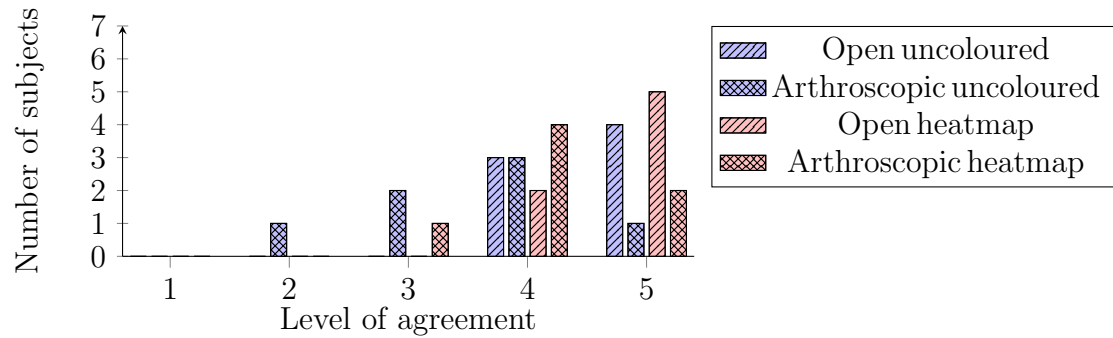


Figure 5.8: Level of agreement (1 = strongly disagree, 5 = strongly agree) to the statement “I was confident that I scanned all parts of the surface that I needed to scan”.

Chapter 6

Discussion

Our results have shown that surface meshes can be produced to within 1.0 mm RMS error in open and arthroscopic scans on plastic models. The duration of the scanning process included on average 56 seconds for data acquisition and 2 seconds for surface generation. Subjects responded favourably to the proposed system.

Some specific findings within the results will be discussed in Section 6.1. There were some limitations to this study, which will be further discussed in Section 6.2, though we do not believe these had a major effect on this study.

6.1 Specific Findings

6.1.1 Open Scans Compared to Arthroscopic Scans

Arthroscopic scans produced significantly higher RMS errors (0.97 ± 0.58 mm) than open scans (0.61 ± 0.36 mm). We speculate this was at least partially due to the reported difficulty in orienting the digitizing probe's reference marker toward the tracker (Figure 5.7b) in arthroscopic scans. This may have caused subjects to be unable to reach certain regions on the scanning surface, resulting in decreased

confidence of having scanned all necessary regions (Figure 5.8), and also a perception of greater difficulty in performing the scan (Figure 5.7c). In addition, the reference marker may have been held obliquely to the tracker, which could lead to increased tracking error compared to open scans.

In addition, the simulated skin may have put pressure on the shaft of the digitizing probe, causing it to bend.

Although the result is statistically significant, it is unclear whether it is clinically important.

6.1.2 Uncoloured Scans Compared to Heatmap Scans

No significant change was found in RMS error between uncoloured scans (0.78 ± 0.52 mm) and heatmap scans (0.77 ± 0.52 mm), or in questionnaire responses. This implies that the confidence heatmap provided no additional value to the subjects.

One subject described the heatmap as “distracting”. This subject may have had sufficient experience to identify accurate shapes, and believed that the heatmap did not provide any additional information.

6.1.3 Effect of Data Acquisition Duration

There was no clear correlation between data acquisition duration and surface mesh RMS error (Figure 5.5). As the point density increased, we believe the amount of new information provided by each incoming point was less valuable. It would seem that 30 seconds of data acquisition (or approximately 600 points) can be sufficient, except in cases where the point cloud does not cover the entire scanning surface.

6.1.4 Ease of Using the Digitizing Probe

Every subject agreed that it was easy to learn how to use the digitizing probe (Figure 5.7a).

Subjects reported that it was more difficult to use the digitizing probe in an arthroscopic scan (Figure 5.7c). This may have been a result of difficulties orienting the digitizing probe's reference marker toward the tracker.

6.1.5 Surface Generation Failures

Discontinuous Surfaces

Several of the surface meshes contained discontinuous surfaces which follow the shape of part of the scanning surface, then resume on the incorrect side of the offset surface (Figure 5.2a). All of the face normals are facing one way. We believe that this occurred because only a single, global projection ray was used to filter faces based on their normals in Section 3.2.5. This prompted some of the changes to the surface generation method proposed in Appendix C. These proposed changes are included in an appendix because they are speculative and have not yet been validated in a user study.

Outlier Detection

Outlier detection featured too many false positives and false negatives. False negatives became especially evident in cases where the surface mesh spanned regions clearly outside the intended scanning surface (Figure 5.2b). We observed in offline analysis that false positives occurred frequently (we subjectively estimate about 5%), but the effect of this (if any) was not noticeable. The *neighborCountThreshold* variable was

set too low to filter out some dense regions of outliers, and the *neighborCountRadius* was too low to capture sparse regions of inliers on the surface of the scanning surface. We address this as well in Appendix C.

6.2 Limitations

6.2.1 Parameter Selection

As mentioned previously, parameters were chosen based on data sets collected by Subject 1 (Section 3.4.1). A larger number of subjects for determining parameter selection would have been ideal, but this was infeasible due to the limited availability of subjects.

We also note that the accuracy of the surface mesh is sensitive to this parameter selection, as evidenced by improved outlier detection in Appendix C compared to the results presented in the body of this thesis. We suspect that it is probably possible to find a better selection of parameters, and this should be investigated in future work.

6.2.2 Deviations from Validation Protocol

During one of Subject 3’s first arthroscopic uncoloured scan (site 3), the surface mesh was previewed with the confidence heatmap, due to operator error. Although the subject reported this may have had a “small” effect on scanning, the heatmap feature had not yet been explained to the subject. We did not believe that this mistake had an effect on the outcome of the study.

During practice scans, the previews were occasionally shown with the confidence heatmap instead of being uncoloured, again due to operator error. As before, we do not expect this to have any effect on the results.

On a few occasions during the user study, the generated surface meshes contained inconsistencies that were caused by the surface generation method (Figure 5.2). When this occurred, the operator advised the subject that the inconsistency was a result of the surface generation method, and was not necessarily caused by insufficient data acquisition.

6.2.3 Sources of Error from Methods

Data Acquisition

The tracker we used has an expected error of 0.25 mm RMS. This error will also affect the calibration, which will propagate into the collected point cloud. The digitizing probe shaft can bend if too much pressure is applied, which will also cause the calibration to be inaccurate. We believe that outlier detection and point cloud smoothing (MLS projection) performed during the surface generation step may have reduced the effect of these types of errors.

Surface Generation

During MLS projection (Section 3.2.2), points are inherently smoothed. This may affect the surface generation method's ability to reconstruct fine details and roughness in the scanning surface.

Validation Protocol

The 3D printer used to print the scanning and reference model may introduce some amount of inaccuracy if the model deforms during cooling after printing. We did not notice any deformation on visual inspection.

The surface meshes needed to be aligned to the ground truth because the point clouds were collected in a different coordinate frame. The iterative closest point algorithm [5] is not perfect, and we expected some error from this alignment.

Arthroscope Head Lock

Five subjects reported that the arthroscope head lock affected their performance. Two subjects reported that the effect of the lock was “small”. Therefore the arthroscope head lock may have had a slight effect on the study.

6.2.4 Initial Surface Orientation

The operator made the decision to manually reverse the initial surface normals based on the output of the surface generation. This is a subjective determination, but the operator was familiar with the anatomy and confident of the decisions. In cases where the normals were reversed, the surface generation was run again. While seemingly minor, this subjective decision and potential increase in running time would not be acceptable in the operating room. We propose an automatic method for making this decision in Appendix C.

6.2.5 Code Errors

During stages 3 and 5 of surface generation, an indexing error caused point classifications (inside/outside) to be inaccurate. In stage 3 (filtering points sufficiently outside the surface), we expect this error had only a minimal effect on surface mesh quality; most points were too close to the initial surface for this determination to matter. In stage 5 (face filtering), this may have caused errors in computing the expected

normal, and faces may have been incorrectly filtered.

Chapter 7

Conclusions

In this thesis, we have contributed a method by which to generate patient-specific surface meshes of the femur intraoperatively using the digitizing probe. Our research objective was to construct meshes using our method with an RMS error of less than 1.0 mm. We conducted a user study in which seven orthopaedic surgeons and residents scanned a rapid-prototyped model. These results show that we achieved our objective: We were able to generate most surface meshes with submillimeter accuracy. The process of acquiring data lasted less than a minute on average, and the surface generation method ran for 2 seconds on average. We believe that the reported durations would be acceptable for clinical use. Our results suggest that the proposed confidence heatmap did not have an effect on surface mesh quality. Our method may allow anatomical scanning, surgical planning, and guided execution to all occur within the operating room without any prior preparation.

Future Work

We have proposed changes to mitigate some of the shortcomings of our method (Appendix C). Although a brief analysis shows that these changes improve surface meshes,

there remains much work that can be done to extend our method:

- The scanning model could be scanned via the conventional method (CT followed by segmentation) in order to directly compare our results with the state of the art.
- The parameter selection could be optimized.
- Different methods for data acquisition and surface generation may be explored in order to further reduce error and scanning duration.
- An *in vivo* experiment could be done to make a clinical evaluation for this method.
- It may be possible to apply this method in scanning other anatomical structures, such as the shoulder and hip.

Bibliography

- [1] M Alexa, J Behr, D Cohen-Or, S Fleishman, D Levin, and CT Silva. Computing and rendering point set surfaces. *IEEE Transactions on Visualization and Computer Graphics*, 9(1):3–15, 2003.
- [2] KS Arun, TS Huang, and SD Blostein. Least-squares fitting of two 3-D point sets. *IEEE Transactions on Pattern Analysis and Machine Intelligence*, 9(5):698–700, 1987.
- [3] DC Barratt, CSK Chan, PJ Edwards, GP Penney, M Slomczykowski, TJ Carter, and DJ Hawkes. Instantiation and registration of statistical shape models of the femur and pelvis using 3D ultrasound imaging. *Medical Image Analysis*, 12(3):358–374, 2008.
- [4] M Berger, JA Levine, LG Nonato, G Taubin, and CT Silva. A benchmark for surface reconstruction. *ACM Transactions on Graphics*, 32(2):20, 2013.
- [5] PJ Besl and ND McKay. A method for registration of 3-D shapes. *IEEE Transactions on Pattern Analysis and Machine Intelligence*, 14(2):239–256, 1992.

- [6] FL Bookstein. Principal warps: Thin-plate splines and the decomposition of deformations. *IEEE Transactions on Pattern Analysis and Machine Intelligence*, 11(6):567–585, 1989.
- [7] J Canny. A computational approach to edge detection. *IEEE Transactions on Pattern Analysis and Machine Intelligence*, 8(6):679–698, 1986.
- [8] CSK Chan, DC Barratt, PJ Edwards, GP Penney, M Slomczykowski, TJ Carter, and DJ Hawkes. Cadaver validation of the use of ultrasound for 3D model instantiation of bony anatomy in image guided orthopaedic surgery. In *Medical Image Computing and Computer-Assisted Intervention*, pages 397–404, 2004.
- [9] CSK Chan, PJ Edwards, and DJ Hawkes. Integration of ultrasound-based registration with statistical shape models for computer-assisted orthopaedic surgery. *Journal of Medical Imaging*, 5032:414–424, 2003.
- [10] W Chang. Surface reconstruction from points. Depth examination review, University of California, 2006.
- [11] A Ciampalini, P Cignoni, C Montani, and R Scopigno. Multiresolution decimation based on global error. *The Visual Computer*, 13(5):228–246, 1997.
- [12] BJ Cole and M D’Amato. Autologous chondrocyte implantation. *Operative Techniques in Orthopaedics*, 11(2):115 – 131, 2001.
- [13] TF Cootes, CJ Taylor, DH Cooper, and J Graham. Active shape models-their training and application. *Computer Vision and Image Understanding*, 61(1):38–59, 1995.

- [14] V Dessenne, S Lavallée, R Julliard, P Cinquin, and R Orti. Computer assisted knee anterior cruciate ligament reconstruction: first clinical tests. In *Computer Vision, Virtual Reality and Robotics in Medicine*, pages 476–480, 1995.
- [15] AW Fitzgibbon. Robust registration of 2D and 3D point sets. *Image and Vision Computing*, 21(13):1145–1153, 2003.
- [16] M Fleute, S Lavalle, and R Julliard. Incorporating a statistically based shape model into a system for computer-assisted anterior cruciate ligament surgery. *Medical Image Analysis*, 3:209–222, 1999.
- [17] M Fleute and S Lavallée. Nonrigid 3-D/2-D registration of images using statistical models. In *Medical Image Computing and Computer-Assisted Intervention*, pages 138–147, 1999.
- [18] M Fleute, S Lavallée, and L Desbat. Integrated approach for matching statistical shape models with intra-operative 2D and 3D data. In *Medical Image Computing and Computer-Assisted Intervention*, pages 364–372, 2002.
- [19] P Foroughi, E Boctor, MJ Swartz, RH Taylor, and G Fichtinger. Ultrasound bone segmentation using dynamic programming. In *IEEE Symposium on Ultrasonics*, pages 2523–2526, 2007.
- [20] P Foroughi, D Song, G Chintalapani, RH Taylor, and G Fichtinger. Localization of pelvic anatomical coordinate system using us/atlas registration for total hip replacement. In *Medical Image Computing and Computer-Assisted Intervention*, pages 871–879, 2008.

- [21] J Grondin Lazazzera. Predicting femoral geometry from anatomical features. Master’s thesis, Queen’s University, 2014.
- [22] M Han and T Kanade. Creating 3D models with uncalibrated cameras. In *IEEE Workshop on Applications of Computer Vision*, pages 178–185, 2000.
- [23] L Hangody and E Balo. Autologous osteochondral mosaicplasty. In Vicente Sanchis-Alfonso, editor, *Anterior Knee Pain and Patellar Instability*, pages 483–494. Springer London, 2011.
- [24] M Hayashibe, N Suzuki, and Y Nakamura. Laser-scan endoscope system for intraoperative geometry acquisition and surgical robot safety management. *Medical Image Analysis*, 10(4):509–519, 2006.
- [25] T Heimann and H Meinzer. Statistical shape models for 3D medical image segmentation: A review. *Medical Image Analysis*, 13(4):543–563, 2009.
- [26] H Hoppe, T DeRose, T Duchamp, J McDonald, and W Stuetzle. Surface reconstruction from unorganized points. *ACM SIGGRAPH*, 26(2):71–78, 1992.
- [27] M Hu, G Penney, M Figl, P Edwards, F Bello, R Casula, D Rueckert, and D Hawkes. Reconstruction of a 3D surface from video that is robust to missing data and outliers: Application to minimally invasive surgery using stereo and mono endoscopes. *Medical Image Analysis*, 16(3):597–611, 2012.
- [28] T Hüfner, J Geerling, M Kfuri, A Gänsslen, M Citak, T Kirchhoff, AH Sott, and C Krettek. Computer assisted pelvic surgery: registration based on a modified external fixator. *Computer Aided Surgery*, 8(4):192–197, 2003.

- [29] J Inoue, M Kunz, MB Hurtig, SD Waldman, and AJ Stewart. Automated planning of computer assisted mosaic arthroplasty. In *Medical Image Computing and Computer-Assisted Intervention*, pages 267–274, 2011.
- [30] R Julliard, S Lavalle, and V Dessenne. Computer assisted reconstruction of the anterior cruciate ligament. *Clinical Orthopaedics and Related Research*, 354:57, 1998.
- [31] M Kazhdan, M Bolitho, and H Hoppe. Poisson surface reconstruction. In *Eurographics Symposium on Geometry Processing*, 2006.
- [32] J Kowal, CA Amstutz, M Caversaccio, and L-P Nolte. On the development and comparative evaluation of an ultrasound B-mode probe calibration method. *Computer Aided Surgery*, 8(3):107–119, 2003.
- [33] M Kunz, S Devlin, RH Gong, J Inoue, SD Waldman, M Hurtig, P Abolmaesumi, and J Stewart. Prediction of the repair surface over cartilage defects: A comparison of three methods in a sheep model. In *Medical Image Computing and Computer-Assisted Intervention*, pages 75–82, 2009.
- [34] M Kunz, SM Devlin, MB Hurtig, SD Waldman, JF Rudan, DD Bardana, and AJ Stewart. Image-guided techniques improve the short-term outcome of autologous osteochondral cartilage repair surgeries: An animal trial. *Cartilage*, 4(2):153–164, 2013.
- [35] A Lasso, T Heffter, A Rankin, C Pinter, T Ungi, and G Fichtinger. PLUS: Open-source toolkit for ultrasound-guided intervention systems. *IEEE Transactions on Biomedical Engineering*, (to appear), 2014.

- [36] Z Mao, K Park, K Lee, and X Li. Robust surface reconstruction of teeth from raw pointsets. *International Journal for Numerical Methods in Biomedical Engineering*, 30(3):382–396, 2014.
- [37] MI Miga, DM Cash, Z Cao, Galloway Jr.RL, BM Dawant, and WC Chapman. Intraoperative registration of the liver for image-guided surgery using laser range scanning and deformable models. *Journal of Medical Imaging*, 5029:350–359, 2003.
- [38] T Minas and S Nehrer. Current concepts in the treatment of articular cartilage defects. *Orthopedics*, 20(6):525–538, 1997.
- [39] T Minas and L Peterson. Advanced techniques in autologous chondrocyte transplantation. *Clinics in Sports Medicine*, 18(1):13–44, 1999.
- [40] R Nabeyama, S Matsuda, H Miura, T Mawatari, T Kawano, and Y Iwamoto. The accuracy of image-guided knee replacement based on computed tomography. *Journal of Bone & Joint Surgery, British Volume*, 86(3):366–371, 2004.
- [41] Northern Digital. Passive polaris spectra user guide, March 2008. Revision 4.
- [42] GP Penney, PJ Edwards, AP King, JM Blackall, PG Batchelor, and DJ Hawkes. A stochastic iterative closest point algorithm (stochastICP). In *Medical Image Computing and Computer-Assisted Intervention*, pages 762–769, 2001.
- [43] KH Pridie and G Gordon. A method of resurfacing osteoarthritic knee joints. *Journal of Bone and Joint Surgery-British Volume*, 41(3):618–619, 1959.

- [44] KT Rajamani, MA Styner, H Talib, G Zheng, LP Nolte, and MA Gonzlez Ballester. Statistical deformable bone models for robust 3D surface extrapolation from sparse data. *Medical Image Analysis*, 11(2):99 – 109, 2007.
- [45] K Rathnayaka, T Sahama, MA Schuetz, and B Schmutz. Effects of CT image segmentation methods on the accuracy of long bone 3D reconstructions. *Medical Engineering & Physics*, 33(2):226–233, 2011.
- [46] K Rönn, N Reischl, E Gautier, and M Jacobi. Current surgical treatment of knee osteoarthritis. *Arthritis*, 2011:454873, 2011.
- [47] D Rueckert, LI Sonoda, C Hayes, DLG Hill, MO Leach, and DJ Hawkes. Non-rigid registration using free-form deformations: application to breast MR images. *IEEE Transactions on Medical Imaging*, 18(8):712–721, 1999.
- [48] RB Rusu, N Blodow, Z Marton, A Soos, and M Beetz. Towards 3D object maps for autonomous household robots. In *IEEE/RSJ International Conference on Intelligent Robots and Systems*, pages 3191–3198, 2007.
- [49] RB Rusu and S Cousins. 3D is here: Point Cloud Library (PCL). In *IEEE International Conference on Robotics and Automation*, 2011.
- [50] O Sadowsky, G Chintalapani, and RH Taylor. Deformable 2D-3D registration of the pelvis with a limited field of view, using shape statistics. In *Medical Image Computing and Computer-Assisted Intervention*, pages 519–526, 2007.
- [51] M Sati, H Staubli, Y Bourquin, M Kunz, and L-P Nolte. Real-time computerized in situ guidance system for ACL graft placement. *Computer Aided Surgery*, 7(1):25–40, 2002.

- [52] C Schmalz, F Forster, A Schick, and E Angelopoulou. An endoscopic 3D scanner based on structured light. *Medical Image Analysis*, 16(5):1063–1072, 2012.
- [53] S Sebastyan. Computer-assisted mosaic arthroplasty: A femur model trial. Master’s thesis, Queen’s University, 2013.
- [54] Smith & Nephew. Osteochondral grafting using the smith & nephew MOSAIC-PLASTY ® System, September 2005.
- [55] JR Steadman, KK Briggs, JJ Rodrigo, MS Kocher, TJ Gill, and WG Rodkey. Outcomes of microfracture for traumatic chondral defects of the knee: average 11-year follow-up. *Arthroscopy: The Journal of Arthroscopic & Related Surgery*, 19(5):477–484, 2003.
- [56] E Stindel, JL Briard, P Merloz, S Plaweski, F Dubrana, C Lefevre, and J Troccaz. Bone morphing: 3D morphological data for total knee arthroplasty. *Computer Aided Surgery*, 7(3):156–168, 2002.
- [57] N Sugano, T Sasama, Y Sato, Y Nakajima, T Nishii, K Yonenobu, S Tamura, and T Ochi. Accuracy evaluation of surface-based registration methods in a computer navigation system for hip surgery performed through a posterolateral approach. *Computer Aided Surgery*, 6(4):195–203, 2001.
- [58] R Szeliski and S Lavalle. Matching 3-D anatomical surfaces with non-rigid deformations using octree-splines. *International Journal of Computer Vision*, 18:171–186, 1996.

- [59] J Weese, M Kaus, C Lorenz, S Lobregt, R Truyen, and V Pekar. Shape constrained deformable models for 3D medical image segmentation. In *Information Processing in Medical Imaging*, pages 380–387, 2001.
- [60] RJ 3rd Williams and HW Harnly. Microfracture: indications, technique, and results. *Instructional Course Lectures*, 56:419–428, 2006.
- [61] C Wu, SG Narasimhan, and B Jaramaz. A multi-image shape-from-shading framework for near-lighting perspective endoscopes. *International Journal of Computer Vision*, 86(2-3):211–228, 2010.
- [62] G Wyvill, C McPheevers, and B Wyvill. Data structure for soft objects. *The Visual Computer*, 2(4):227–234, 1986.
- [63] PA Yushkevich, J Piven, HC Hazlett, RG Smith, S Ho, JC Gee, and G Gerig. User-guided 3D active contour segmentation of anatomical structures: significantly improved efficiency and reliability. *Neuroimage*, 31(3):1116–1128, 2006.
- [64] G Zheng, MAG Ballester, M Styner, and L-P Nolte. Reconstruction of patient-specific 3D bone surface from 2D calibrated fluoroscopic images and point distribution model. In *Medical Image Computing and Computer-Assisted Intervention*, pages 25–32, 2006.
- [65] G Zheng, X Dong, KT Rajamani, X Zhang, M Styner, RU Thoranaghatte, L-P Nolte, and MAG Ballester. Accurate and robust reconstruction of a surface model of the proximal femur from sparse-point data and a dense-point distribution model for surgical navigation. *IEEE Transactions on Biomedical Engineering*, 54(12):2109–2122, 2007.

- [66] G Zheng and S Schumann. 3D reconstruction of a patient-specific surface model of the proximal femur from calibrated x-ray radiographs: A validation study. *Medical Physics*, 36(4):1155–1166, 2009.
- [67] G Zheng, S Schumann, and MAG Ballester. An integrated approach for reconstructing a surface model of the proximal femur from sparse input data and a multi-resolution point distribution model: an in vitro study. *International Journal of Computer Assisted Radiology and Surgery*, 5(1):99–107, 2010.

Appendix A

Informed Consent



**QUEEN'S UNIVERSITY HEALTH SCIENCES & AFFILIATED TEACHING HOSPITALS RESEARCH
ETHICS BOARD-DELEGATED REVIEW**

May 22, 2014

Mr. Thomas Vaughan
School of Computing
Queen's University

Dear Mr. Vaughan

Study Title: SCOMP-013-14 Bone shape determination on a computer using a pointing device

File # 6012480

Co-Investigators: Dr. J. Stewart

I am writing to acknowledge receipt of your recent ethics submission. We have examined the protocol, confidentiality agreement, questionnaire, recruitment letter, letter of information and consent form for your project (as stated above) and consider it to be ethically acceptable. This approval is valid for one year from the date of the Chair's signature below. This approval will be reported to the Research Ethics Board. Please attend carefully to the following listing of ethics requirements you must fulfill over the course of your study:

Reporting of Amendments: If there are any changes to your study (e.g. consent, protocol, study procedures, etc.), you must submit an amendment to the Research Ethics Board for approval. Please use event form: HSREB Multi-Use Amendment/Full Board Renewal Form associated with your post review file # **6012480** in your Researcher Portal (https://eservices.queensu.ca/romeo_researcher/)

Reporting of Serious Adverse Events: Any unexpected serious adverse event occurring locally must be reported within 2 working days or earlier if required by the study sponsor. All other serious adverse events must be reported within 15 days after becoming aware of the information. Serious Adverse Event forms are located with your post-review file **6012480** in your Researcher Portal (https://eservices.queensu.ca/romeo_researcher/)

Reporting of Complaints: Any complaints made by participants or persons acting on behalf of participants must be reported to the Research Ethics Board within 7 days of becoming aware of the complaint. Note: All documents supplied to participants must have the contact information for the Research Ethics Board.

Annual Renewal: Prior to the expiration of your approval (which is one year from the date of the Chair's signature below), you will be reminded to submit your renewal form along with any new changes or amendments you wish to make to your study. If there have been no major changes to your protocol, your approval may be renewed for another year.

Yours sincerely,

Albert Z. Clark.

Chair, Health Sciences Research Ethics Board
May 22, 2014

Investigators please note that if your trial is registered by the sponsor, you must take responsibility to ensure that the registration information is accurate and complete

Letter of Information
Bone shape determination on a computer using a pointing device

This research is being conducted by Thomas Vaughan under the supervision of Dr James Stewart, in the School of Computing at **Queen's University** in Kingston, Ontario.

What is this study about? The purpose of this research is to evaluate methods that may allow the generation of a bone's shape on a computer intraoperatively. During this study, you will use an optically tracked surgical tool and will position the surgical tool to identify points on the surface of several simulated plastic bone models, and several cadaver bones. You will be asked to fill out questionnaires regarding your age, surgical experience, handedness, and your general impressions about the tools under study. The study will require a single visit of duration no more than two hours. Because we are using a cadaver, there is a risk of biohazardous contamination. Every attempt will be made to minimize this risk according to normal Kingston General Hospital regulations regarding biohazardous materials. There are no other known physical, psychological, economic, or social risks associated with this study.

Is my participation voluntary? Yes. Although it would be greatly appreciated if you would answer all material as frankly as possible, you should not feel obliged to answer any material that you find objectionable or that makes you feel uncomfortable. You may withdraw at any time.

What will happen to my responses? We will keep your responses confidential. Only experimenters will have access to this information. To help us ensure confidentiality, please do not put your name on any of the research study answer sheets. The data may also be published in professional journals or presented at scientific conferences, but any such presentations will be of general findings and will never breach individual confidentiality. Should you be interested, you are entitled to a copy of the findings.

Will I be compensated for my participation? No, there is no compensation for participation in this study.

What if I have concerns? Any questions about study participation may be directed to Thomas Vaughan at vaughan@cs.queensu.ca, or Dr James Stewart at jstewart@cs.queensu.ca. Any ethical concerns about the study may be directed to the Chair of the Health Sciences Research Ethics Board at clarkaf@queensu.ca or 613-533-6081.

Again, thank you. Your interest in participating in this research study is greatly appreciated.

Consent Form
Bone shape determination on a computer using a pointing device

Name (please print clearly): _____

1. I have read the Letter of Information and have had any questions answered to my satisfaction.
2. I understand that I will be participating in the study called "Bone shape determination on a computer using a pointing device" conducted by Thomas Vaughan under Dr James Stewart's supervision at the School of Computing at **Queen's University** in Kingston, Ontario. I understand that this means that I will be asked to use an optically tracked pointing device to indicate to a computer 3D points that are on the surfaces of plastic bone models and cadaver bones. I understand that I will be asked to repeat this process for several sites of interest. I understand that I will be asked general questions about my age, surgical experience, handedness, and my impressions of the tools under study. I understand the risks associated with the use of cadavers in this study, and that every attempt will be made to minimize this risk according to normal Kingston General Hospital regulations regarding biohazardous materials.
3. I understand that my participation in this study is voluntary and I may withdraw at any time. I understand that every effort will be made to maintain the confidentiality of the data now and in the future. Only experimenters in the Computer Assisted Surgical Interventions Laboratory will have access to this area. The data may also be published in professional journals or presented at scientific conferences, but any such presentations will be of general findings and will never breach individual confidentiality. Should I be interested, I am entitled to a copy of the findings.
4. I am aware that if I have any questions, concerns, or complaints, I may contact Thomas Vaughan (vaughan@cs.queensu.ca); project supervisor, Dr. James Stewart (533-3156, jstewart@cs.queensu.ca); Head of the School of Computing (533-3184, akl@cs.queensu.ca), or the Chair of the Health Sciences Research Ethics Board (533-6081, clarkaf@queensu.ca) at Queen's University.

I have read the above statements and freely consent to participate in this research:

Signature: _____ Date: _____

Appendix B

User Study Questionnaire

Questionnaire for surgeons and residents participating in the study:

Bone shape determination on a computer using a pointing device

Identifier (to be used by the researchers only): _____

The following section is to be completed before the experiment

Please indicate your age: _____

Are you a surgeon or a resident?

Surgeon / Resident

Please indicate how many years of experience you have as a fellow or surgeon, or which year of residency you are currently in:

_____ Years as a fellow or surgeon / Year of residency

Are you right-handed, left-handed, or ambidextrous?

Right / Left / Ambidextrous

The following section is to be completed after the experiment

For each of the following statements, please indicate on a scale of 1 to 5 your level of agreement (where 1 indicates you strongly disagree, and 5 indicates you strongly agree):

Learning how to use the digitizing probe was easy.

(Strongly disagree) 1 2 3 4 5 (Strongly agree)

Comment (optional):

It was easy to keep the digitizing probe's dynamic reference body (reflective markers) within the line of sight of the infrared tracker.

Open: (Strongly disagree) 1 2 3 4 5 (Strongly agree)

Closed: (Strongly disagree) 1 2 3 4 5 (Strongly agree)

Comment (optional):

I was confident that I scanned all parts of the surface that I needed to scan.

Open White: (Strongly disagree) 1 2 3 4 5 (Strongly agree)

Open Colour: (Strongly disagree) 1 2 3 4 5 (Strongly agree)

Closed White: (Strongly disagree) 1 2 3 4 5 (Strongly agree)

Closed Colour: (Strongly disagree) 1 2 3 4 5 (Strongly agree)

Comment (optional):

Scanning with the digitizing probe was easy.

Open: (Strongly disagree) 1 2 3 4 5 (Strongly agree)

Closed: (Strongly disagree) 1 2 3 4 5 (Strongly agree)

Comment (optional):

I found the surface colouring according to a reliability metric was useful.

Open: (Strongly disagree) 1 2 3 4 5 (Strongly agree)

Closed: (Strongly disagree) 1 2 3 4 5 (Strongly agree)

Comment (optional):

Is there anything else you would like to tell us?

Appendix C

Adjustments to Surface Generation

The subjective decision to reverse initial surface normals is undesirable. In addition, there were several failed surface generations, and we have identified two causes (Section 6.1.5). The proposed changes to the surface generation method here are intended to address these issues. We describe these changes, then run the modified surface generation method on the point clouds we collected during the user study to verify that the changes are valid.

C.1 Initial Surface Orientation

A known point outside the scanning surface must be collected or defined. We project rays from the centroid of each face to the known outside point. For each face, the dot product between the face normal and ray direction is calculated. If the dot product is negative more often than it is positive, then all of the mesh normals are reversed to face the other way.

C.2 Discontinuous Surfaces

The implementation described in Section 3.2.5 assumes that all faces in the desired surface mesh has normals facing one global direction. We remove this assumption, and instead use local directions.

As in the original implementation, we compute the offset surface from the refined surface. There are still two stages, one based on normal comparison, and one to reject faces which were far from input points.

C.2.1 Face Filtering: Normal Comparison

We must evaluate whether each face is outside or inside the refined surface. For each face in the offset surface, a ray from the nearest surface point on the refined surface to the centroid of the offset face is calculated. Then, the dot product between the ray and the surface normal at the nearest surface point is computed. The face is outside the refined surface and removed if and only if the dot product is positive.

C.2.2 Face Filtering: Near Existing Points

Each point from the filtered input point cloud (prior to MLS projection) is projected to the nearest surface point on the offset surface. We compute the *convex hull* of the projected points. We used the VTK class *vtkDelaunay3D* with a large offset value to approximate the convex hull. Any faces from the remaining offset surface which were outside and sufficiently far from the convex hull were discarded (we refer to this threshold distance once again as *thresholdConvexHullDistance*, and set it to 1 mm). It is important to also include regions which were within a close distance to the convex hull, since the convex hull may not have captured the intended faces in

concave regions.

C.3 Outlier Detection

We collected datasets with point density similar to the user study, while attempting to induce outliers. We then optimized the *neighborCountRadius* and *neighborCountThreshold* parameters to detect the outliers and retain the majority of valid points. The new values are recorded below (Table 5.1).

Parameter name	value
<i>neighborCountRadius</i>	15 points
<i>neighborCountThreshold</i>	4 mm

Table C.1: Modified parameter selection.

C.4 Effect of Proposed Changes

We performed our modified surface generation and the same validation protocol on the input point clouds we collected during the user study. Most of the surface generation failures (12 out of 13 failures) did not recur, though there were still stray faces in some cases (Figure C.1a). We compared our new surface meshes (Figure C.1a and Figure C.1b) with the earlier result (Figure 5.2a and Figure 5.2b, respectively). Figure C.2 shows the failing case.

We also noted a decrease in mean RMS error, with RMS errors of 0.54 ± 0.26 mm for open scans, and 0.91 ± 0.59 mm for arthroscopic scans. The difference in RMS errors between open and arthroscopic scans is still significant ($p < 0.0001$).

We compared our results to those from Section 5 using the Wilcoxon signed rank test for paired data. Comparing the new open scan RMS errors to those in Section 5

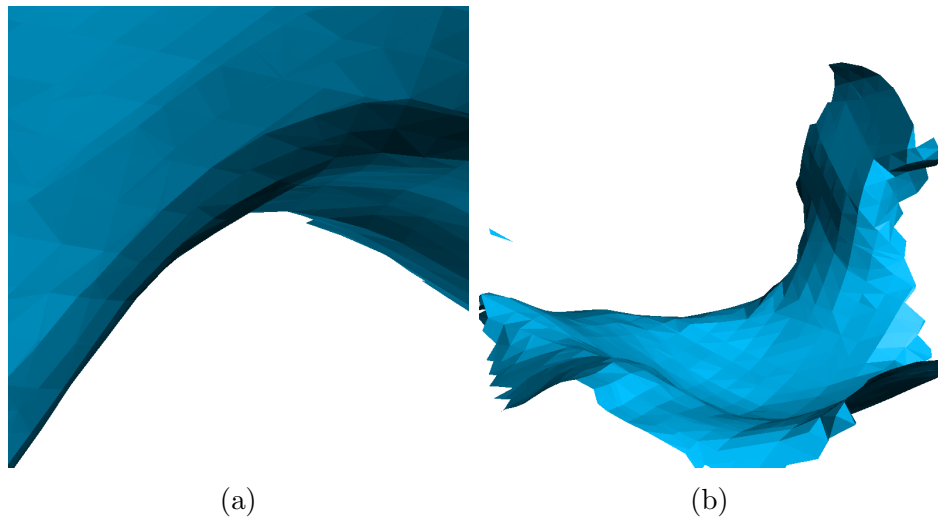


Figure C.1: Surface meshes using the proposed changes to surface generation. These previously failed (Figure 5.2).

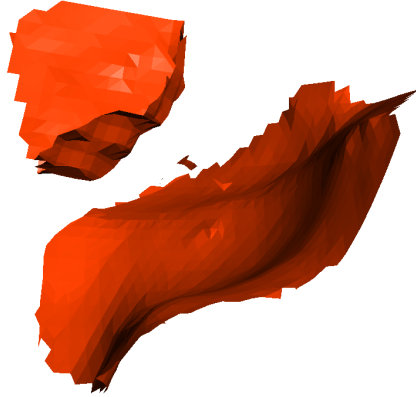


Figure C.2: A failed case using the proposed modified method. The faces in the top left are not part of the scanning surface.

$(0.61 \pm 0.36 \text{ mm})$, the result is significantly improved ($p = 0.0025$). Comparing the new arthroscopic scan RMS errors to those in Section 5 ($0.97 \pm 0.58 \text{ mm}$), the result is significantly improved ($p = 0.019$).

These results are not reported in the main thesis because the modifications were made after the user study had been done. A new study would have to be done to

validate the changes.